Research Article

Synapse Weakening-Induced Caspase-3 Activity Confers Specificity to Microglia-Mediated Synapse Elimination

Zhou Yu[1], Andrian Gutu[1], Namsoo Kim[1], Erin K. O'Shea[1]

1. Howard Hughes Medical Institute, Ashburn, United States

During brain development, synapses are initially formed in excess and are later eliminated in an activity-dependent manner, with weak synapses being preferentially removed. Previous studies identified glia as mediators of synapse removal, but it is unclear how glia specifically target weak synapses. Here we show that, in the developing mouse visual pathway, inhibiting synaptic transmission induces postsynaptic activation of caspase-3. Caspase-3 is essential for synapse elimination driven by both spontaneous and experience-dependent neural activity. Synapse weakening-induced caspase-3 activation determines the specificity of synapse elimination mediated by microglia but not astrocytes. Furthermore, in a mouse model of Alzheimer's disease, caspase-3 deficiency protects against synapse loss induced by amyloid-β deposition. Our results reveal caspase-3 activation as a key step in activity-dependent synapse elimination during development and synapse loss in neurodegeneration.

Zhou Yu and Andrian Gutu contributed equally to this work.

Corresponding authors: Zhou Yu, zyu3@bwh.harvard.edu; Erin K. O'Shea, osheae@hhmi.org

Synapse elimination is the process in which excess synapses formed early during brain development are subsequently eliminated to form mature circuits[1][2][3]. A key feature of synapse elimination is that the outcome critically depends on both spontaneous and experience-driven neural activity, and less active synapses are preferentially removed[2][4][5]. Previous studies have established that microglia and astrocytes, two major glial cell types of the brain, engage in synapse engulfment by using phagocytic receptors to detect 'eat-me' signals displayed on synapses[6][7][8][9][10][11][12][13][14]. Although both microglia- and astrocyte-mediated synapse elimination are known to be activity-dependent[7][10], it is unclear how the intrinsic strength of a synapse is converted into external molecular cues that can be

recognized by glial cells to guide the selective removal of weaker synapses. A recent study proposed a molecular mechanism for activity-dependent synapse elimination in which the JAK2-STAT1 pathway is activated in inactive callosal projection neurons and regulates the removal of synapses and axons[15]. However, the JAK-STAT pathway canonically functions through transcriptional regulation[16], which affects entire cells. If not all synapses made by a neuron are destined for removal[3], activation of the JAK2-STAT1 pathway alone may not provide sufficient elimination specificity. Therefore, other unidentified, locally-effective mechanisms likely exist that confer elimination specificity at the synapse level.

Caspase-3 is a protease crucial for the execution of apoptosis[17]. In hippocampal neurons, transient activation of caspase-3 is required for long-term depression (LTD), a form of synaptic plasticity that induces long-lasting decreases in synaptic strength[18]. Caspase-3 activation is also known to trigger the display of 'eat-me' signals on apoptotic cells, facilitating their clearance by phagocytes through the engagement of phagocytic receptors[19][20]. These findings led us to hypothesize that caspase-3 may link synapse weakening with glial recognition and subsequent synapse removal. Although caspases were previously implicated in dendrite pruning in metamorphosis, degeneration-like axon elimination, and the regulation of hippocampal spine density[21][22][23][24], the role of caspase-3 in synapse elimination in response to neural activity was not clear. In this work, we identify caspase-3 as a pivotal molecule that is activated in postnatal development in dendritic compartments upon synaptic weakening and is necessary to direct microglia to selectively eliminate weak synapses. Furthermore, we discovered that caspase-3 deficiency protects against amyloid-β-induced synapse loss in a mouse model of Alzheimer's disease, highlighting its significance not only in development synapse elimination but also in adult neurodegenerative diseases.

Synapse inactivation induces postsynaptic caspase-3 activity

We chose the mouse retinogeniculate visual pathway as a model system to study synapse elimination[25]. In mice, retinal ganglion cells (RGCs) in each eye send out axons to form retinogeniculate synapses with relay neurons in the dorsal lateral geniculate nuclei (dLGN) of the thalamus on both sides of the brain (**Fig. S1**)[25]. The majority of RGC axons from each eye innervate the contralateral (on the side opposite to the originating eye) dLGN while a smaller fraction innervate the ipsilateral (on the same side as the originating eye) dLGN (**Fig. S1**)[25]. Regions in each dLGN innervated by the two eyes initially overlap but later segregate into eye-specific territories (**Fig. S1**). This segregation process is a hallmark of retinogeniculate

pathway development at the morphological level and depends on synapse elimination and spontaneous RGC activity[25][26][27].

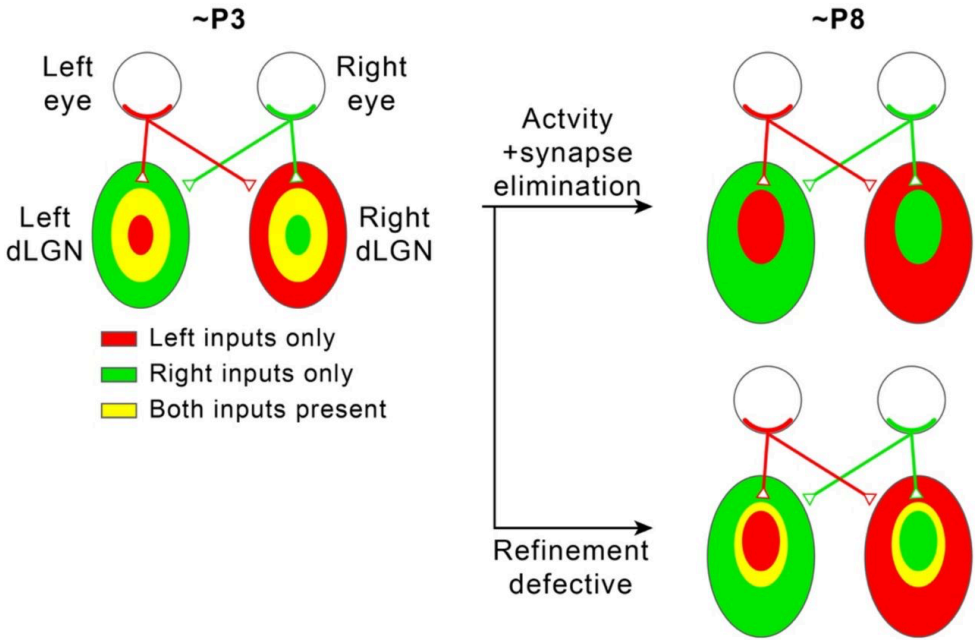


Figure S1. Segregation of eye-specific territories in the mouse retinogeniculate pathway. In the mouse retinogeniculate pathway, retinal ganglion cells (RGCs) in the retina of each eye innervate relay neurons in both the contralateral (opposite side as the originating RGC) dorsal lateral geniculate nucleus (dLGN) and the ipsilateral (same side from the originating RGC) dLGN to form retinogeniculate synapses (upper right). Within each dLGN, the majority of retinogeniculate synapses receive inputs from the contralateral eye, while the minority receive inputs from the ipsilateral eye (upper right). At the age of P3, regions in each dLGN receiving inputs from each of the two eyes overlap significantly (left). Through a process that requires synapse elimination and spontaneous RGC activity, these regions are refined into non-overlapping eye-specific territories by the age of P8 (upper right). If the refinement process is defective because neural activity or synapse elimination is disrupted, eye-specific territories fail to completely segregate, and regions innervated by the two eyes remain overlapping (lower right).

To investigate the role of caspase-3 in activity-dependent synapse elimination, we first needed to establish a method that could manipulate the strength of a selective subset of retinogeniculate synapses. For this purpose, we used adeno-associated-virus (AAV) to deliver a construct expressing tetanus toxin light chain (TeTxLC) under the control of the neuron-specific human synapsin promoter (AAV-hSyn-TeTxLC) (**Fig.**

1A)[28]. *In utero* intraocular injection of AAV-hSyn-TeTxLC at embryonic day 15 (E15) leads to TeTxLC expression in RGCs by the time of birth, blocking neurotransmitter release at retinogeniculate synapses by cleaving synaptobrevin[28][29]. As anterograde tracers and controls, we used AAV to express a fluorescent protein (mTurquiose2, eGFP, or tdTomato, depending on the experiment) either alone or together with TeTxLC (**Fig. 1A**). To validate our method, we injected AAV-hSyn-TeTxLC into the right eye of wildtype E15 embryos and analyzed eye-specific territories at postnatal day 8 (P8) (see **Fig. S2** and text associated with **Fig. 3** for details of the analysis), when the segregation process is largely complete[25]. Consistent with previous results[26][27], inactivating right eye-associated retinogeniculate synapses led to contraction of right eye-specific territories and expansion of left eye-specific territories relative to control animals (**Fig. S3A** and **S3B**). In addition, segregation of eye-specific territories in TeTxLC-injected mice was defective (**Fig. S3C** and **S3D**), confirming that our method potently inactivated synapses and perturbed activity-dependent refinement of the retinogeniculate pathway.

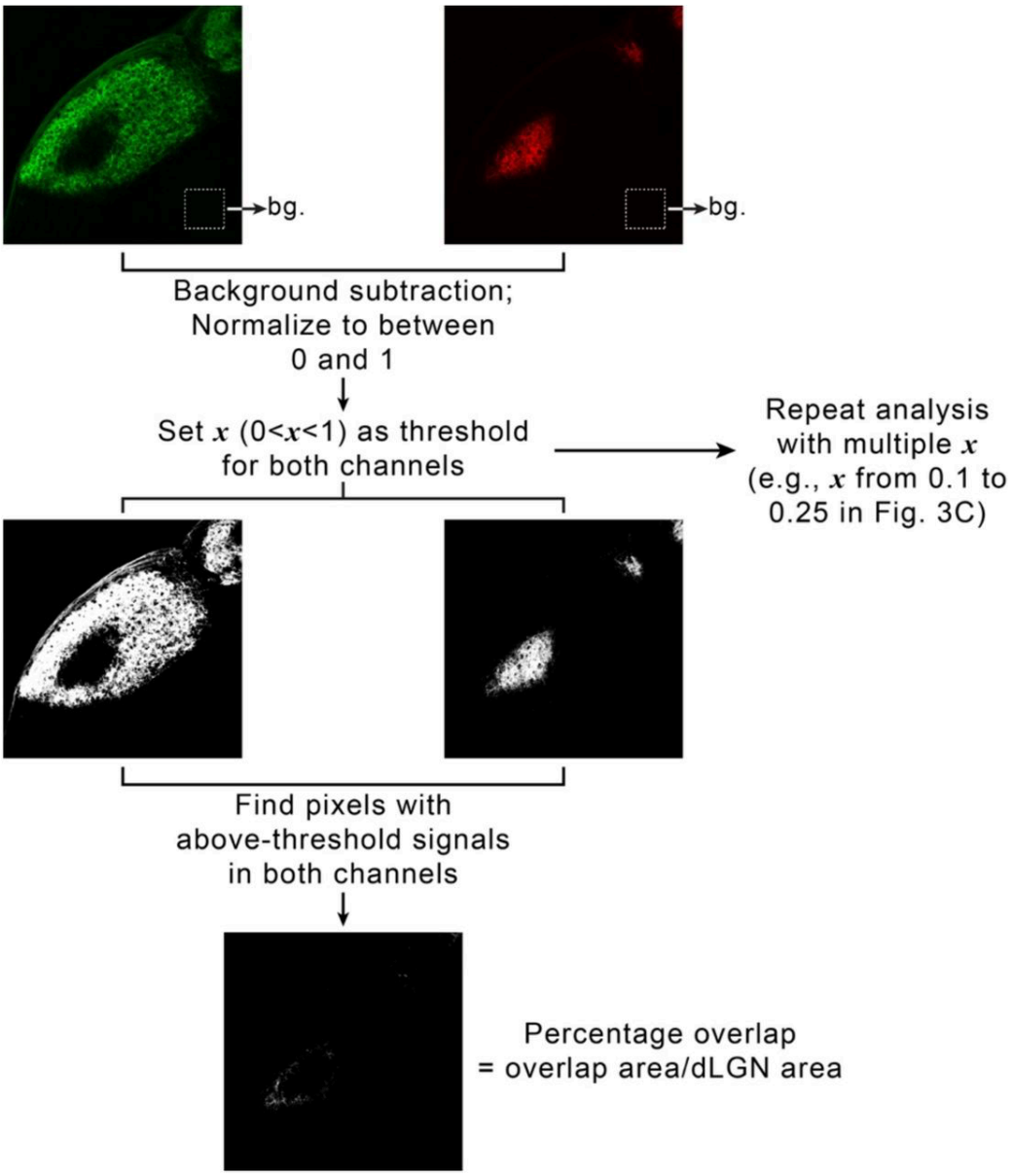
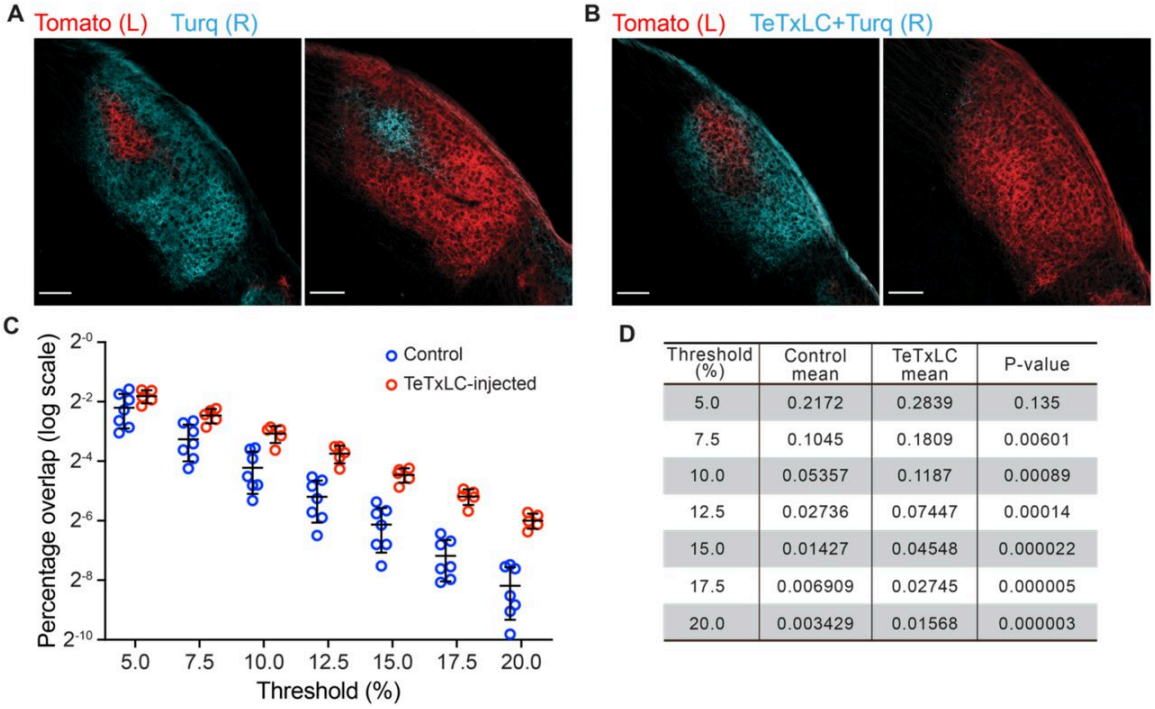


Figure S2. Quantifying eye-specific segregation with multi-threshold overlap analysis. For each dLGN, RGC inputs from the two eyes were imaged using separate fluorescence channels. A small area in the thalamus outside of each dLGN was chosen, and average signal intensity in each channel within that area was calculated and used as background (upper panel). For each channel, background was subtracted, and signals were normalized to between 0 and 1. To calculate overlap between eye-specific territories, a threshold, *x*, was chosen between 0 and 1 and applied to both channels (middle panel). The overlap between eye-specific territories were defined as the set of pixels with above-threshold signals in both channels. Percentage overlap was then calculated as the ratio between the area of the dLGN where eye-specific territories overlapped and the total area of the dLGN (lower

panel). To avoid introducing biases by artificially selecting one threshold, we repeated the analysis with a set of increasingly stringent thresholds (e.g., from 0.1 to 0.25 in **Fig. 3C** and **3D**).



Threshold (%)	Control mean	TeTxLC mean	P-value
5.0	0.2172	0.2839	0.135
7.5	0.1045	0.1809	0.00601
10.0	0.05357	0.1187	0.00089
12.5	0.02736	0.07447	0.00014
15.0	0.01427	0.04548	0.000022
17.5	0.006909	0.02745	0.000005
20.0	0.003429	0.01568	0.000003

Figure S3. Blocking spontaneous RGC activity in one eye with TeTxLC disrupts eye-specific segregation in the retinogeniculate pathway. (**A** and **B**) Confocal images of P8 left dLGN (left panels) and right dLGN (right panels) of an animal receiving control injections (**A**) and an animal receiving TeTxLC injection in the right eye (**B**). Eye-specific regions were labeled with tdTomato (red, left eye input) and mTurquiose2 (cyan, right eye input). Right eye territory (cyan) contracted and left eye territory (red) expanded in TeTxLC-injected animals (**B**) compared to controls (**A**). Scale-bars: 100 μm. (**C**) Quantification of overlap between eye-specific territories in dLGN of P8 control and TeTxLC-injected animals. Analysis was done at multiple thresholds to avoid biases introduced with threshold selection. Note that percentage overlap is displayed on a log scale. For details on the analysis, see **Fig. S2** and text associated with **Fig. 3**. n=7 for control animals and 5 for TeTxLC-injected animals. Mean and S.D. are shown. (**D**) Statistics of the overlap analysis at multiple thresholds. Fold difference and the statistical significance of the difference in percentage overlap between the two groups of animals increased as threshold increased. P-values were calculated from two-tailed t-tests. We did not implement multiple comparison corrections as values at different thresholds are derived from the same dataset and are not independent.

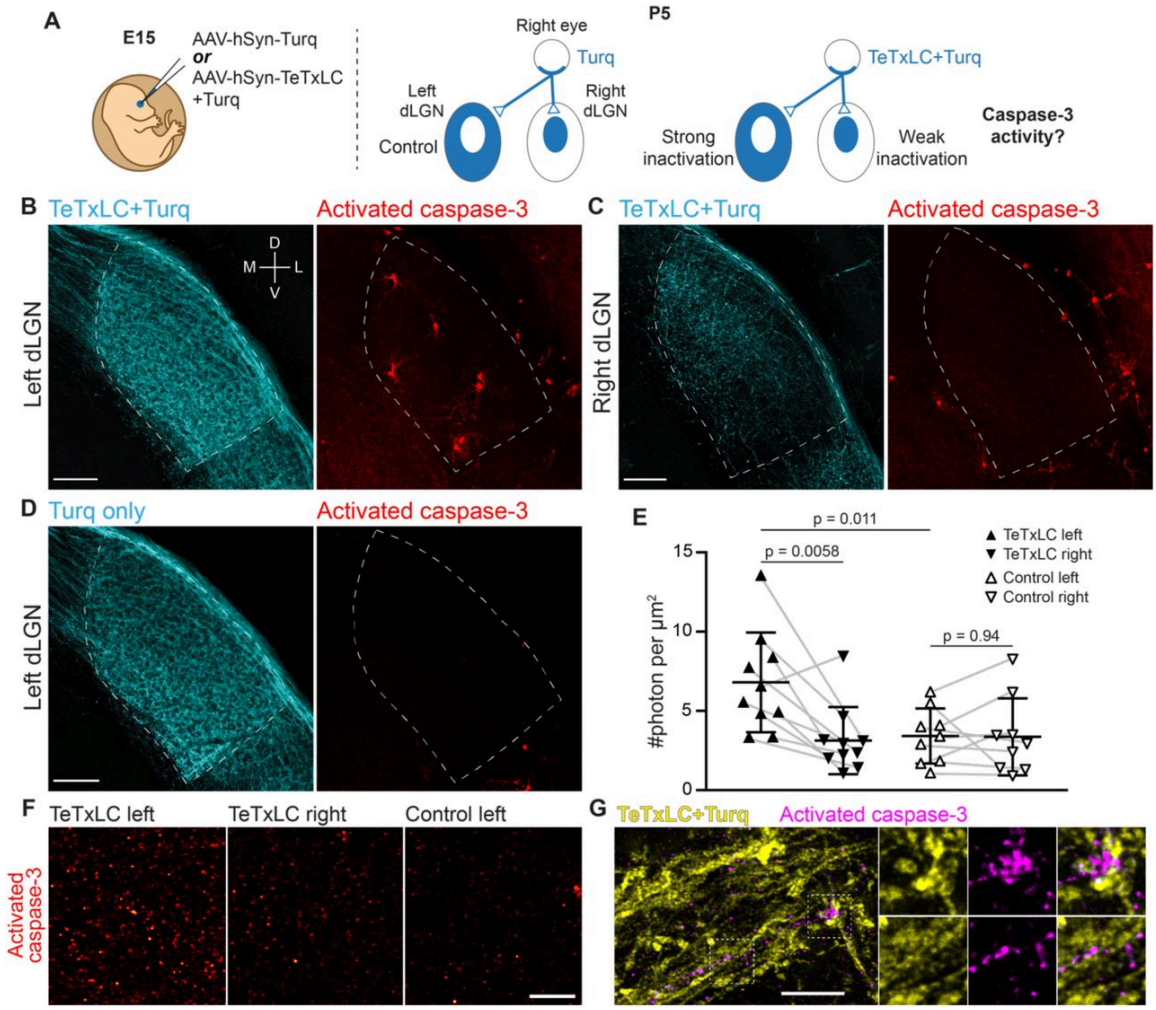


Figure 1. Inactivation of retinogeniculate synapses induces caspase-3 activity. (**A**) Schematics of experimental setup. AAVs expressing tetanus toxin light chain (TeTxLC) and/or mTurquiose2 (Turq) were injected into the right eye of E15 mice (left). By P5, retinogeniculate synapses in dLGN were inactivated to varying extents depending on injection and side (right). (**B**-**D**) Confocal images of Turq (left panels) and activated caspase-3 (right panels) in left dLGN (**B**) and right dLGN (**C**) of a TeTxLC-injected P5 animal and in left dLGN of a control P5 animal (**D**). Images from the same fluorescent channel were adjusted to the same contrast. Dotted lines delineate dLGN boundaries. The compass in **B** marks tissue orientation. Scale-bars: 100 μm. D, dorsal; V, ventral; M, medial; L, lateral. (**E**) Quantification of caspase-3 activity in indicated dLGNs. Activated caspase-3 signals in each dLGN (highlighted areas in **B**-**D**) were summed and normalized to dLGN area. Each point represents the result from one dLGN. Data from two dLGNs of the same animal were paired for analysis (grey lines). n=10 for TeTxLC-injected animals and n=9 for control animals. Mean and standard deviation (S.D.) are shown. P-values were calculated from two-tailed t-tests (paired when applicable). (**F**) Example images showing punctate caspase-3 activities in ventral-medial regions of indicated dLGNs. Images were adjusted to the same contrast. Scale-bar: 20 μm. (**G**) High-resolution images of dLGN showing TeTxLC-expressing RGC axons (yellow) and

doi.org/10.32388/TD1OXF

activated caspase-3 (magenta). Two regions of interest (dotted squares) are magnified to illustrate that caspase-3 activity was found juxtaposing TeTxLC-expressing axon terminals but not within them. Scale-bar: 5 μm.

Is caspase-3 activated in response to synapse weakening? To address this question, we injected AAV-hSyn-TeTxLC into the right eyes of E15 embryos and looked for caspase-3 activation in dLGNs of TeTxLC-injected mice at the age of P5 (a time when synapse elimination is most active) (**Fig. 1A**)[7][25]. TeTxLC expression causes a widespread inactivation of retinogeniculate synapses and enhances potential synapse inactivation-induced caspase-3 activity. We measured caspase-3 activity by detecting the cleaved and active form of caspase-3 through immunohistochemistry[17]. If synapse inactivation leads to caspase-3 activation, we would expect higher levels of caspase-3 activity in dLGNs with more inactivated synapses (**Fig. 1A**). In agreement with this hypothesis, normalized caspase-3 activity in the left dLGN of right eye TeTxLC-injected animals (**Fig. 1B** and **1E**) was significantly higher compared to that in the right dLGN of right eye TeTxLC-injected animals (**Fig. 1C** and **1E**) and compared to that in the left dLGN of Turq-injected control animals (**Fig. 1D** and **1E**). We did not detect differences in caspase-3 activity between the right dLGN of right eye TeTxLC-injected animals and the dLGN of control animals (**Fig. 1C**, **1D** and **1E**), presumably due to low levels of synaptic inactivation in the former and/or insufficient signal-to-background ratio. Reassuringly, caspase-3 activities in left and right dLGN of control animals were comparable (**Fig. 1E**), suggesting that surgical manipulation and viral transduction did not contribute to caspase-3 activation. These findings support the model that inactivation of retinogeniculate synapses induces caspase-3 activation.

Does inactivation of retinogeniculate synapses activate caspase-3 pre-synaptically in RGCs or post-synaptically in dLGN relay neurons? Caspase-3 activity in dLGNs of TeTxLC-injected mice was present either as discrete, punctate signals (**Fig. 1F**) or as staining of the entire cell (**Fig. 1B** and **Fig. S4Bi-iii**). Both types of signals were more abundant in dLGNs with strong synapse inactivation than in control dLGNs (**Fig. 1B**, **1D** and **1F**). Intriguingly, punctate caspase-3 activity was not found within TeTxLC-expressing RGC axons (**Fig. 1G**). Instead, punctate caspase-3 activity closely juxtaposed inactivated axon terminals (**Fig. 1G**) and co-localized with a dendritic marker, MAP2 (**Fig. S4A**). In the case where caspase-3 was activated in entire cells, the cells were positive for nuclear NeuN (**Fig. S4C**) and possessed relatively large round somas and multipolar dendritic arbors (**Fig. S4Bi-iii**), all of which are characteristics of dLGN relay neurons[30][31]. These observations suggest that caspase-3 activation triggered by synapse inactivation occurs predominantly in the dendritic compartments of dLGN relay neurons that are postsynaptic to the

inactivated synapses. It is important to note that the whole-cell caspase-3 activation observed in TeTxLC-inactivated dLGNs is likely a consequence of strong synapse inactivation and is not a normal developmental phenomenon (compare **Fig. 1B** and **1D**). Consistent with this idea, we observed a transitional state of caspase-3 activation where multiple dendrites of a relay neuron were positive for activate caspase-3 without the cell body becoming apoptotic (**Fig. S4Biv**), suggesting that, in TeTxLC-inactivated dLGNs, strong synapse inactivation causes excessive accumulation of caspase-3 activity in dendrites and eventually leads to caspase-3 activation in entire relay neurons, possibly through caspase-3 mediated feedback amplifications of the apoptosis signaling cascade[32].

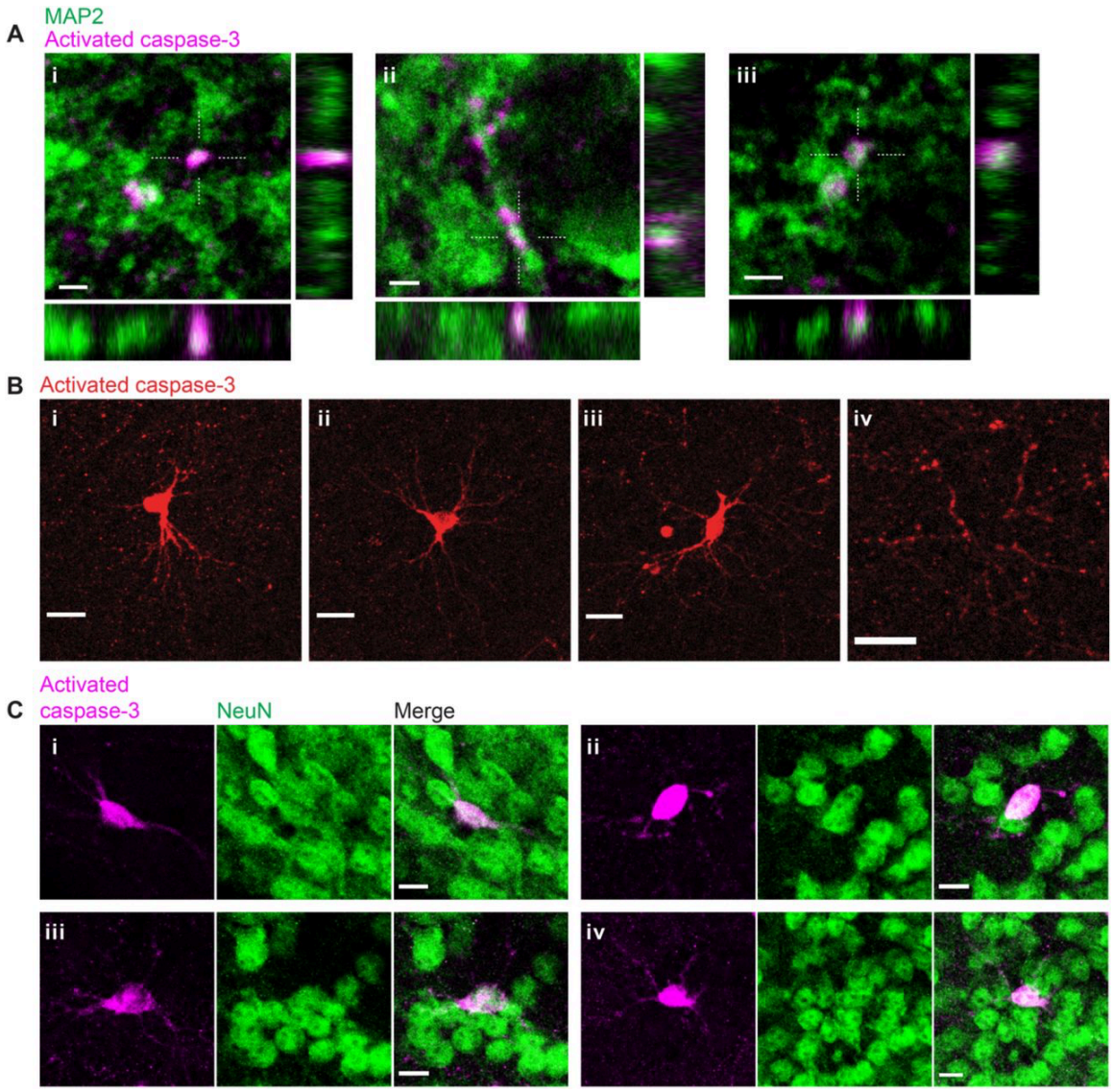


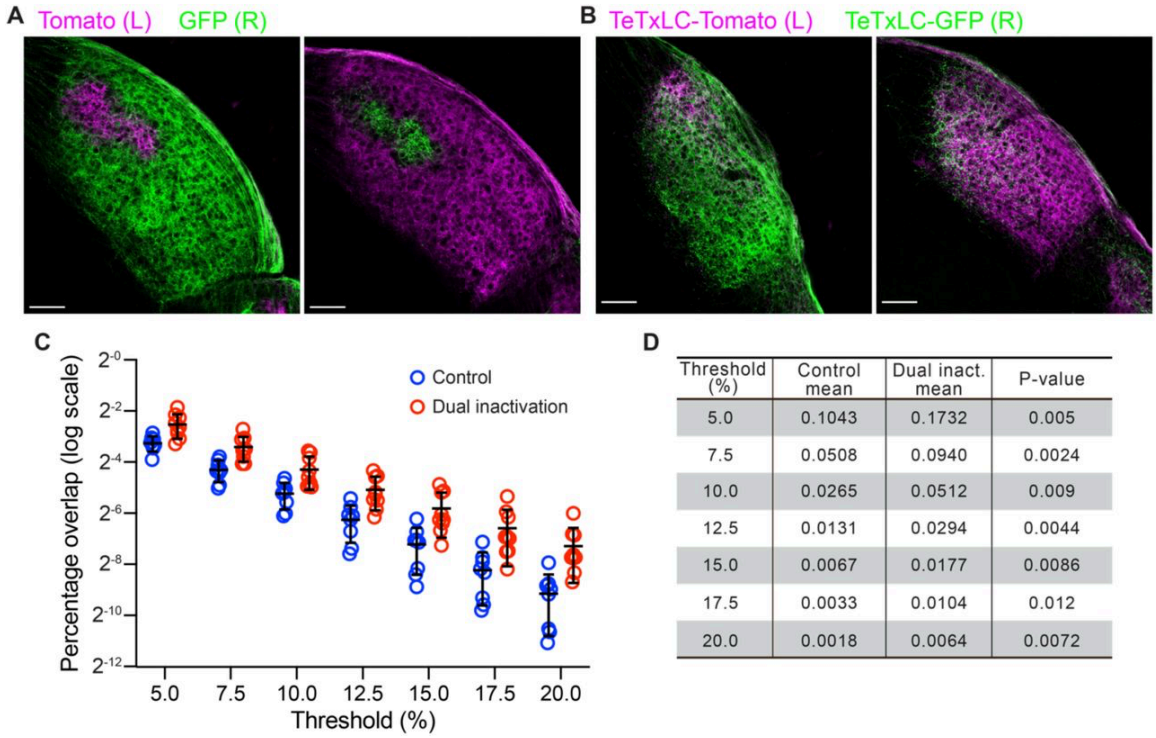
Figure S4. Inactivation of retinogeniculate synapses induces postsynaptic caspase-3 activity in dendritic compartments of dLGN relay neurons. (**A**) High-resolution images of three representative field-of-views (**i**-**iii**) in P5 TeTxLC-expressing dLGNs showing co-localization of punctate caspase-3 activity (magenta) and a dendritic marker, MAP2 (green). Dotted crosses mark x and y positions where the x-z and y-z cross-sections were generated. Scale-bars: 2 μm. (**B**) Example images showing caspase-3 activity in entire neurons (**i**-**iii**) or in multiple dendritic branches (but not the soma) of a neuron (**iv**) in P5 TeTxLC-expressing dLGNs. The neurons positive for active caspase-3 (**i**-**iii**) have relatively large and round somas and multipolar dendritic arbors that are characteristic of dLGN relay neurons. Scale-bars: 20 μm. (**C**) Example images of four representative neurons (**i**-**iv**) in P5 TeTxLC-expressing dLGNs that are positive for active caspase-3 (magenta) and a neuronal nuclear marker, NeuN (green). Scale-bars: 10 μm.

doi.org/10.32388/TD1OXF

Synapse inactivation-induced caspase-3 activation requires synaptic competition

Is synapse inactivation-induced caspase-3 activity a result of synapse inactivation *per se*, or is it a result of competition between inactive and active synapses? Previous studies have either hyperactivated or inactivated RGCs in one of the two eyes while leaving the other eye unperturbed[26][27]. In the scenario involving hyperactivation, both the less active (unperturbed) and the more active (hyperactivated) eye had higher activity than their counterparts in the scenario involving inactivation. However, in both experiments, the dLGN territory of the less active eye contracted while that of the more active eye expanded[26][27], suggesting that relative, rather than absolute, synapse strength determines the outcome of synapse elimination in the retinogeniculate pathway. Consistent with this idea, a recent study demonstrated that elimination of inactive synapses in callosal projections occurred only when other active synapses are present[28][33].

To test if synapse inactivation-induced caspase-3 activation requires synaptic competition, we devised two conditions where either one (single inactivation) or both eyes (dual inactivation) were injected with AAV-hSyn-TeTxLC (**Fig. 2A**). In single inactivation, retinogeniculate synapses originating from different eyes have different strengths and compete within each dLGN (**Fig. 2A**), whereas in dual inactivation, all retinogeniculate synapses are inactivated and no competition occurs (**Fig. 2A**). We first confirmed that, in accordance with previous findings[26][34], inactivating RGCs in both eyes with TeTxLC disrupted segregation of eye-specific regions (**Fig. S5A-D**). We then measured caspase-3 activity in the single- or dual-inactivated dLGNs and in the control dLGN, where retinogeniculate synapses were unperturbed (**Fig. 2A**). Intriguingly, while single inactivation induced significantly higher levels of caspase-3 activity in the dLGN compared to controls (**Fig. 2B** and **2C**), active caspase-3 signal in the dual-inactivated dLGN was not significantly different from the signal in the control dLGN (**Fig. 2B**and **2C**) and was significantly lower than that in the single-inactivated dLGN (**Fig. 2B** and **2C**). Although not reaching statistical significance, caspase-3 activity on average was still higher in the dLGN in dual inactivation than in the control dLGN (**Fig. 2C**), possibly due to incomplete inactivation of retinogeniculate synapses, or competition between retinogeniculate synapses and synapses from other pathways, or additional mechanisms that activate caspase-3 independently of synapse competition. These results suggest that competition between active and inactive retinogeniculate synapses is required to induce caspase-3 activity in dendritic compartments of dLGN relay neurons.



D

Threshold (%)	Control mean	Dual inact. mean	P-value
5.0	0.1043	0.1732	0.005
7.5	0.0508	0.0940	0.0024
10.0	0.0265	0.0512	0.009
12.5	0.0131	0.0294	0.0044
15.0	0.0067	0.0177	0.0086
17.5	0.0033	0.0104	0.012
20.0	0.0018	0.0064	0.0072

Figure S5. Blocking spontaneous RGC activity in both eyes with TeTxLC disrupts eye-specific segregation in the retinogeniculate pathway. (**A** and **B**) Confocal images of the left dLGN (left panels) and right dLGN (right panels) of an animal receiving control injections in both eyes (**A**) and an animal receiving TeTxLC injection in both eyes (**B**). Eye-specific territories were labeled with tdTomato (magenta, left eye input) and eGFP (green, right eye input). In animals injected with TeTxLC in both eyes, territories of the two eyes are similar in size and are more dispersive compared to those in controls, leading to substantial overlap between eye-specific territories. Scale-bars: 100 μm. (**C**) Quantification of overlap between eye-specific territories in the dLGN of control and dual TeTxLC-injected animals. Analysis was done at multiple thresholds to avoid biases introduced with threshold selection. Note that percentage overlap is displayed on a log scale. For details on the analysis, see **Fig. S2** and text associated with **Fig. 3**. n=8 for control animals and n=9 for dually TeTxLC-injected animals. Mean and S.D. are shown. (**D**) Statistics of the overlap analysis at multiple thresholds. Fold difference between the two groups of animals increases as the threshold increases. Statistical significance does not show clear increase with threshold as percentage overlap values are more variable at higher thresholds. P-values were calculated from two-tailed t-tests. We did not implement multiple comparison corrections as values at different thresholds are derived from the same dataset and are not independent.

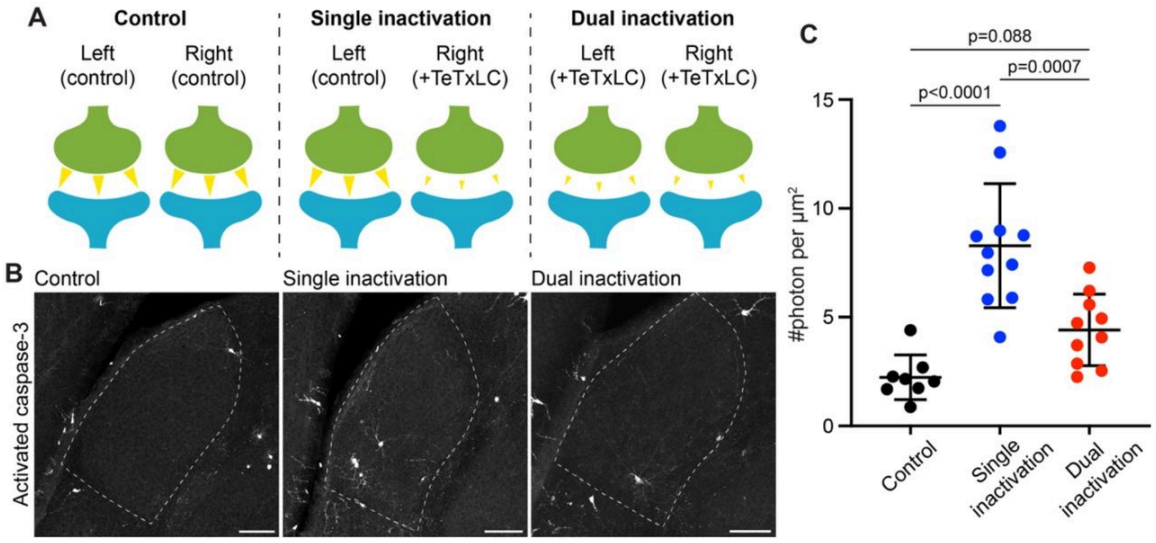
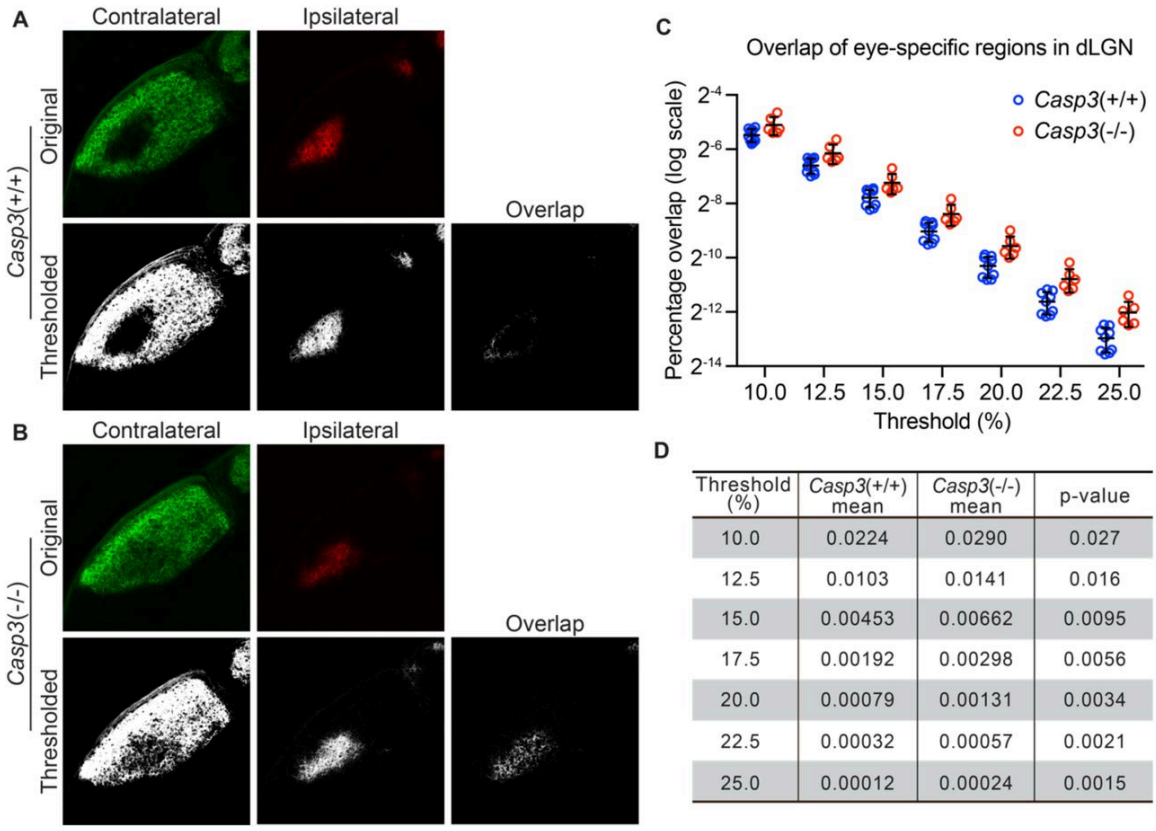


Figure 2. Synapse inactivation-induced caspase-3 activation requires synaptic competition. (**A**) Schematics illustrating different experimental conditions. Presynaptic (green) and postsynaptic (cyan) compartments and synaptic strength (yellow arrowheads) of retinogeniculate synapses are shown. No synapses are inactivated in the control (left); expressing TeTxLC only in right eye inputs results in synapse inactivation and competition (middle); expressing TeTxLC in both eyes results in synapse inactivation but no competition (right). (**B**) Confocal images of dLGNs in the three conditions showing activated caspase-3 signal. The dLGN shown for the single inactivation condition was from the left side. Dotted lines mark dLGN boundaries. Scale-bars: 100 μm. (**C**) Quantification of caspase-3 activity in the dLGN in the indicated conditions. Activated caspase-3 signal in each dLGN were summed and normalized to the dLGN area. For the single inactivation condition, values were from the left dLGN only. For the other two conditions, values from both dLGNs were averaged. n=8 animals for control, n=11 animals for single inactivation, and n=10 animals for dual inactivation. Mean and S.D. are shown. P-values were calculated from Tukey's multiple comparison tests.

Caspase-3 is required for segregation of eye-specific territories

Is synapse inactivation-induced caspase-3 activity important for synapse elimination in the retinogeniculate pathway? To address this question, we investigated whether segregation of eye-specific dLGN territories is defective if caspase-3 activation does not occur. As we were unable to find a Cre-expressing mouse line that satisfactorily depletes caspase-3 in dLGN relay neurons, we used full-body caspase-3 deficient (*Casp3*$^{-/-}$) mice[35][36]. These mice were backcrossed to congenicity on the C57Bl/6J background and were viable, fertile, and did not exhibit overt abnormalities[36].

To measure segregation of eye-specific territories, we injected the eyes of *Casp3*$^{+/+}$ and *Casp3*$^{-/-}$ littermate mice at P9 with fluorophore-conjugated cholera toxin subunit B (CTB), using a different fluorophore for each eye. CTB molecules bind to ganglioside molecules on RGC surfaces and anterogradely label RGC axon terminals[37]. At P10, when CTB labeling and eye-specific segregation were complete[25][38], we collected the brains and imaged eye-specific territories in each dLGN. By visual inspection, eye-specific territories in *Casp3*$^{+/+}$dLGNs overlapped minimally (**Fig. 3A**). By contrast, *Casp3*$^{-/-}$ dLGNs showed clear defects in the separation of eye-specific territories (**Fig. 3B**)[39]. To quantify the overlap between eye-specific territories in an unbiased manner, we applied a set of increasing thresholds to signals from both eyes (**Fig. S2**)[38]. We calculated the percentage overlap of eye-specific territories as the ratio between dLGN area with above-threshold signals from both eyes and the total dLGN area (**Fig. S2** and **Fig. 3C**). Percentage overlap in *Casp3*$^{-/-}$ dLGNs was consistently higher than that in *Casp3*$^{+/+}$ dLGNs across all thresholds (**Fig. 3C** and **D**). Importantly, the fold difference and statistical significance of the difference in percentage overlap between the two groups of animals increased as the cutoff threshold increased (**Fig. 3D**), suggesting the defects observed in *Casp3*$^{-/-}$ animals cannot be attributed to artifacts generated from background noise.



D

Threshold (%)	*Casp3*(+/+) mean	*Casp3*(-/-) mean	p-value
10.0	0.0224	0.0290	0.027
12.5	0.0103	0.0141	0.016
15.0	0.00453	0.00662	0.0095
17.5	0.00192	0.00298	0.0056
20.0	0.00079	0.00131	0.0034
22.5	0.00032	0.00057	0.0021
25.0	0.00012	0.00024	0.0015

Figure 3. Caspase-3 is required for segregation of eye-specific territories. (**A-B**) Representative confocal images of retinogeniculate inputs in the dLGN of P10 wild-type (**A**) and *Casp3*$^{-/-}$ (**B**) mice. Contralateral inputs are labeled with AlexaFlour488 (AF488) conjugated cholera toxin subunit B (CTB) and ipsilateral inputs with AF594-CTB. Original images were thresholded into 0-or-1 images using the Otsu method[34], and the overlap between thresholded contralateral and ipsilateral inputs is shown. (**C**) Percentage overlap between eye-specific territories in wildtype and *Casp3*$^{-/-}$ mice under a series of increasing signal cutoff thresholds. Note that the percentage overlap is plotted on a log scale. Each circle represents one animal. Mean and S.D. are shown. n=9 for wildtype mice and n=6 for *Casp3*$^{-/-}$ mice. (**D**) Mean percentage overlap values in wildtype and *Casp3*$^{-/-}$ mice and p-values of two-tailed t-tests between the two genotypes are listed for each cutoff threshold.

As RGCs are known to undergo extensive apoptosis during the first week of postnatal development[40][41], we wondered if caspase-3 deficiency might block RGC turnover and result in more RGC inputs in the dLGN, thereby confounding the overlap analysis. To address this concern, we quantified the density of RGCs in whole-mount retinae using a RGC marker, RBPMS (**Fig. S6A**)[42]. Reassuringly, RGC densities in retinae of *Casp3*$^{+/+}$ and *Casp3*$^{-/-}$ mice were not different (**Fig. S6B**), indicating that RGC apoptosis still occurred at

doi.org/10.32388/TD1OXF

normal rates in the absence of caspase-3, presumably through redundant mechanisms. Collectively, our findings suggest that caspase-3 is required for normal segregation of eye-specific territories in dLGN.

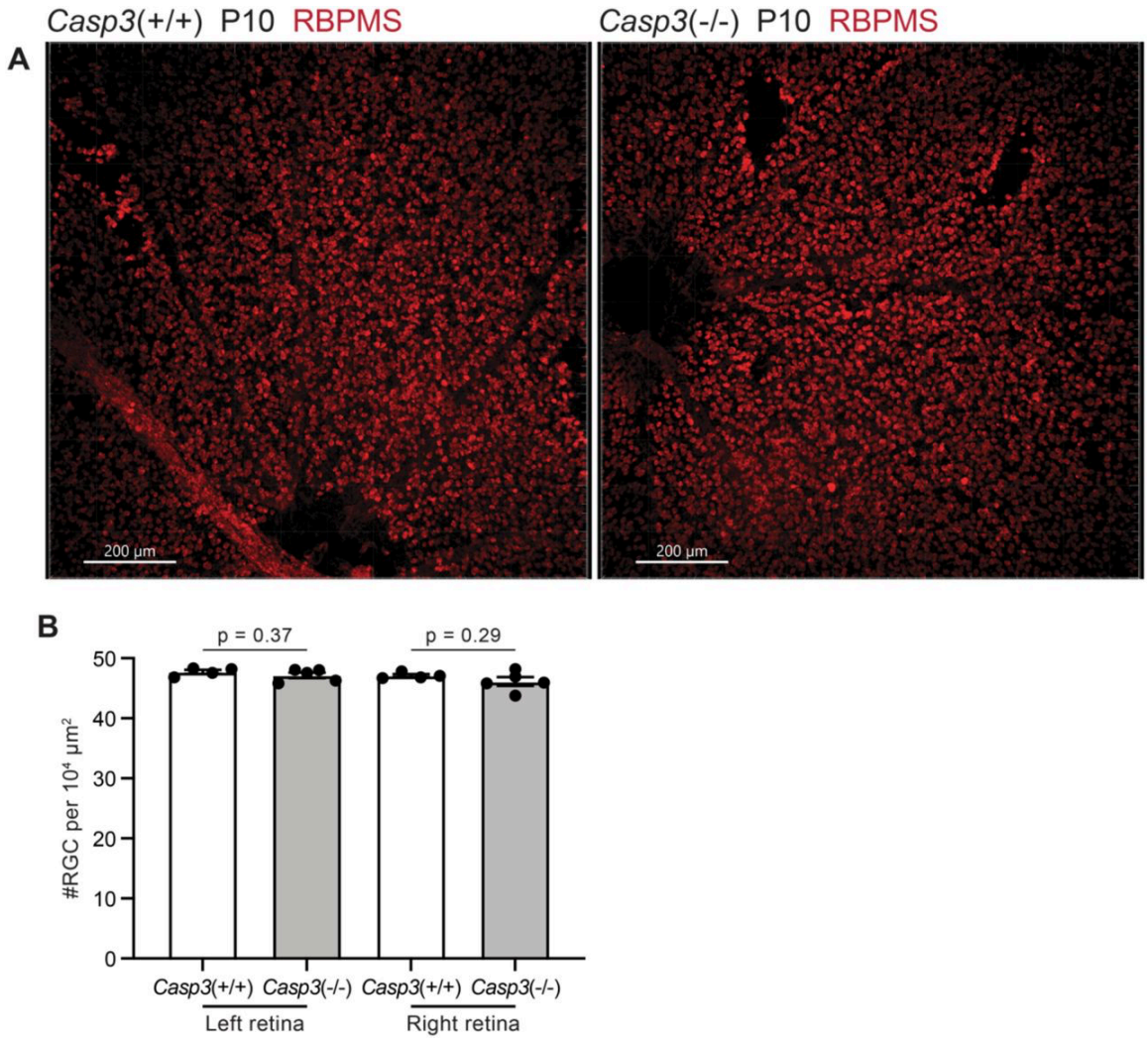


Figure S6. Caspase-3 deficiency does not alter RGC density in the retina. (**A**) Images of whole-mount retinae from P10 *Casp3*$^{+/+}$ (left) and *Casp3*$^{-/-}$ (right) animals. RGCs were labeled in red by immunostaining against an RGC-specific marker, RBPMS (RNA-binding protein with multiple splicing)[37]. The dark regions on the bottom of the left panel and on the left of the right panel are optic discs. Scale-bars: 200 µm. (**B**) Quantification of RGC densities in retinae of P10 *Casp3*$^{+/+}$ and *Casp3*$^{-/-}$ animals. Each point represents one retina. Left and right retinae were analyzed separately. n=4 animals for *Casp3*$^{+/+}$ mice and n=5 animals for *Casp3*$^{-/-}$ mice. Mean and S.D. are shown. P-values were calculated from unpaired two-tailed t-tests.

Caspase-3 is required for retinogeniculate circuit refinement

Segregation of eye-specific territories in the mouse dLGN occurs prior to eye opening (which happens at ~P13) and relies predominantly on spontaneous RGC activity[25]. After eye opening, sensory-dependent RGC activity drives a second phase of refinement at the circuit level[25]. At the time of eye opening, each dLGN relay neuron receives numerous weak RGC inputs. With visual experience, a minority of these inputs are strengthened while other weak inputs are eliminated, so that by P30 only a few (typically ≤3) strong RGC inputs innervate each dLGN relay neuron[25].

To test if caspase-3 is required for visual experience-driven circuit refinement, we prepared acute brain slices from P30 *Casp3*$^{+/+}$ and *Casp3*$^{-/-}$ littermate mice and investigated the electrophysiological properties of retinogeniculate synapses (**Fig. S7A**)[43][44]. We stimulated the optic tract while recording both AMPA receptor (AMPAR)- and NMDA receptor (NMDAR)-mediated excitatory postsynaptic currents (EPSCs) in dLGN relay neurons (**Fig. S7A** and **Fig. 4A-B**). Because each RGC axon has a distinct excitation threshold, as we gradually increase the stimulation intensity on the optic tract, we recruit individual RGC axons in a serial manner (**Fig. S7A**). Excitation of each RGC axon triggers a step increase in the EPSC amplitude (**Fig. S7A**), allowing us to count the number of steps in both AMPAR- and NMDAR-mediated response curves and infer the number of RGC inputs on each relay neuron (**Fig. 4C** and **S8A**). In agreement with previous studies, retinogeniculate circuits in *Casp3*$^{+/+}$ animals were refined, with dLGN relay neurons most frequently receiving 2 strong RGC inputs, and the great majority of neurons receiving no more than 3 inputs (**Fig. 4A**, **4C** and **S8A**). In contrast, RGC input counts of dLGN relay neurons in *Casp3*$^{-/-}$ animals followed a long-tailed distribution that was significant right-shifted from that of *Casp3*$^{+/+}$ animals (**Fig. 4C** and **S8A**). The majority of *Casp3*$^{-/-}$ relay neurons received more than 3 inputs (**Fig. 4B-C** and **S8A**), and many inputs elicited only small increments in EPSC amplitude (**Fig. 4B**). To investigate whether the defects observed in *Casp3*$^{-/-}$ animals could be due to general synaptic dysfunction, we compared AMPAR- and NMDAR-mediated EPSCs in *Casp3*$^{+/+}$ and *Casp3*$^{-/-}$ animals and observed no difference in maximum EPSC amplitude (**Fig. S8B** and **S8C**) or the ratio of the two types of EPSCs (**Fig. S8D**). Additionally, we calculated fiber fraction (FF) as the ratio between the first non-zero response (elicited by a single axon fiber) and the maximum response in each dLGN relay neuron (**Fig. S8E**). FF increases as RGC inputs are strengthened during development[44]. We observed comparable FF values in *Casp3*$^{+/+}$ and *Casp3*$^{-/-}$ animals (**Fig. S8E**), which suggests that defective circuit refinement in *Casp3*$^{-/-}$ animals was not due to lack of RGC input strengthening but instead an inability to eliminate weak inputs.

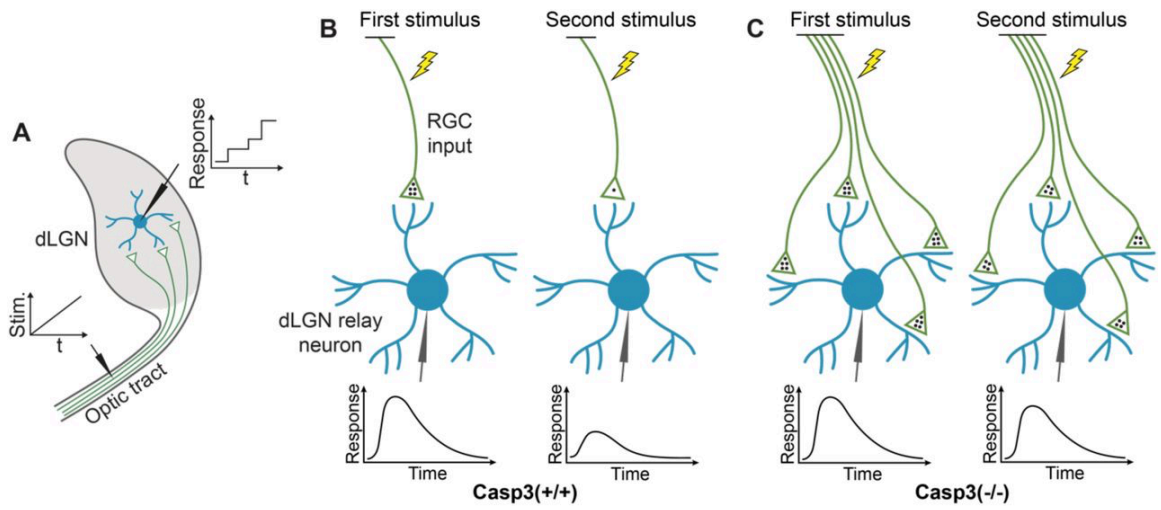


Figure S7. Measuring electrophysiological properties of retinogeniculate synapses. (**A**) Inferring the number of RGC inputs of dLGN relay neurons by measuring stimulation-response curves. To measure relay neuron responses, we prepared acute brain slices from a tilted parasagittal plane in P30 mice[38]. These slice preparations preserved a long segment of the optic tract and a high level of connectivity between RGC axons and dLGN relay neurons[38]. We placed a stimulating electrode on the optic tract and patch-clamped individual dLGN relay neurons with a recording electrode. We stimulated the optic tract with a series of gradually increasing currents and recorded excitatory postsynaptic currents (EPSCs) in relay neurons. At low stimulation intensity, no RGC axons were activated. As the stimulus increased, more and more RGC axons were recruited. As different RGC axons have different excitation thresholds, RGC axons were excited one at a time. Whenever a stimulus activated an RGC axon that did not respond to lower stimuli, a step increase in the relay neuron response was detected, and the increment corresponded to the EPSC evoked by the newly recruited RGC axon. We can therefore infer the number of RGC inputs innervating the relay neuron being recorded by counting the number of steps in the response curve of that relay neuron. t: time. Stim.: stimulation intensity. (**B**-**C**) Inferring the number of release sites from RGC inputs by measuring paired-pulse response ratio (PPR). We stimulated the optic tract with two stimuli separated by a short interval and recorded EPSCs in dLGN relay neurons. The stimulus intensity was chosen to evoke maximum response in the relay neuron. In wildtype mice (**B**), the first stimulus triggers the release of a significant fraction of the readily releasable pool (RRP) of neurotransmitters (black dots), evoking a strong response (left). At the time of the second stimulus, the RRP does not have sufficient time to recover and remains depleted, resulting in a weaker second response (right). PPR can be calculated from this experiment by dividing the peak amplitude of the second response with that of the first. PPR is small in wildtype animals. In caspase-3 deficient mice (**C**), if the number of release sites is increased compared to wildtype animals, the RRP should be larger (left), and a smaller fraction of the RRP is released during the first stimulus, leaving more neurotransmitters available for the second stimulus (right), thereby enhancing the second response and PPR. Note that in this model, we made two assumptions. The first assumption is that the average size of the RRP in

one release site is similar in *Casp3*$^{+/+}$ and *Casp3*$^{-/-}$ mice, which is supported by the comparable fiber fractions (FFs) in the two groups of animals (see **Fig. S8E**). The second assumption is that the number of neurotransmitters released during the first stimulus is similar in *Casp3*$^{+/+}$ and *Casp3*$^{-/-}$ mice (4 dots in the illustration), which is supported by the comparable maximum EPSCs in the two groups of animals (see **Fig. S8B-C**).

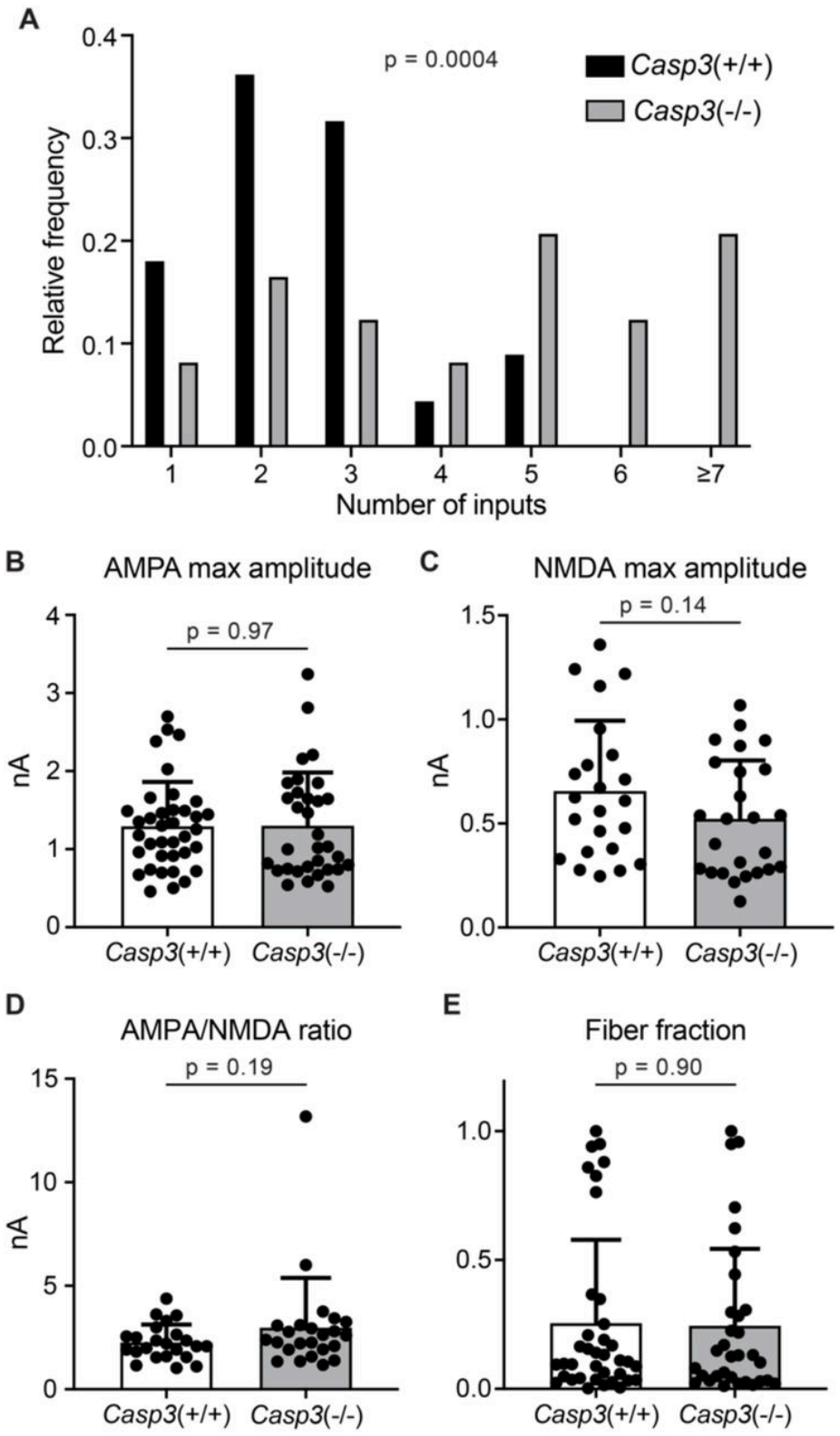


Figure S8. Additional analyses of electrophysiological properties of retinogeniculate synapses in *Casp3*$^{+/+}$ and *Casp3*$^{-/-}$ mice. (**A**) Distribution of RGC input numbers of individual dLGN relay neurons in wildtype and *Casp3*$^{-/-}$ mice measured by counting the

doi.org/10.32388/TD1OXF

number of steps in NMDAR-mediated EPSC response curves (upper right in **Fig. 4A** and **4B**) while blind to genotypes. P-value was calculated from two-tailed t-test. n=22 cells for wildtype mice and n=24 cells for *Casp3*$^{-/-}$ mice. (**B**-**C**) Quantification of maximum amplitudes of AMPAR- (**B**) and NMDAR-mediated (**C**) EPSCs in wildtype and *Casp3*$^{-/-}$ dLGN relay neurons. (**D**) Quantification of the ratio between maximum amplitudes of AMPAR- and NDMAR-mediated EPSCs in wildtype and *Casp3*$^{-/-}$dLGN relay neurons. (**E**) Quantification of fiber fractions in wildtype and *Casp3*$^{-/-}$ dLGN relay neurons. When stimulation on the optic tract is gradually increased, there will be a lowest stimulation intensity at which a non-zero response is first recorded in the relay neuron (see **Fig. S8** for illustration and **Fig. 4** for example data). This first response is presumed to be evoked by the activation of a single RGC axon fiber. Fiber fraction is defined as the ratio between this single-fiber response and the maximum response and ranges from 0 to 1. Only the AMPAR-mediated response is used to calculate fiber fractions. In **B**-**E**, mean and S.D. are shown. In **A**-**E**, p-values were calculated from two-tailed t-tests. In **A**, **C**, and **D**, n = 22 cells for wildtype mice and n=24 cells for *Casp3*$^{-/-}$ mice. In **B** and **E**, n=37 cells for wildtype mice and n=32 cells for *Casp3*$^{-/-}$ mice.

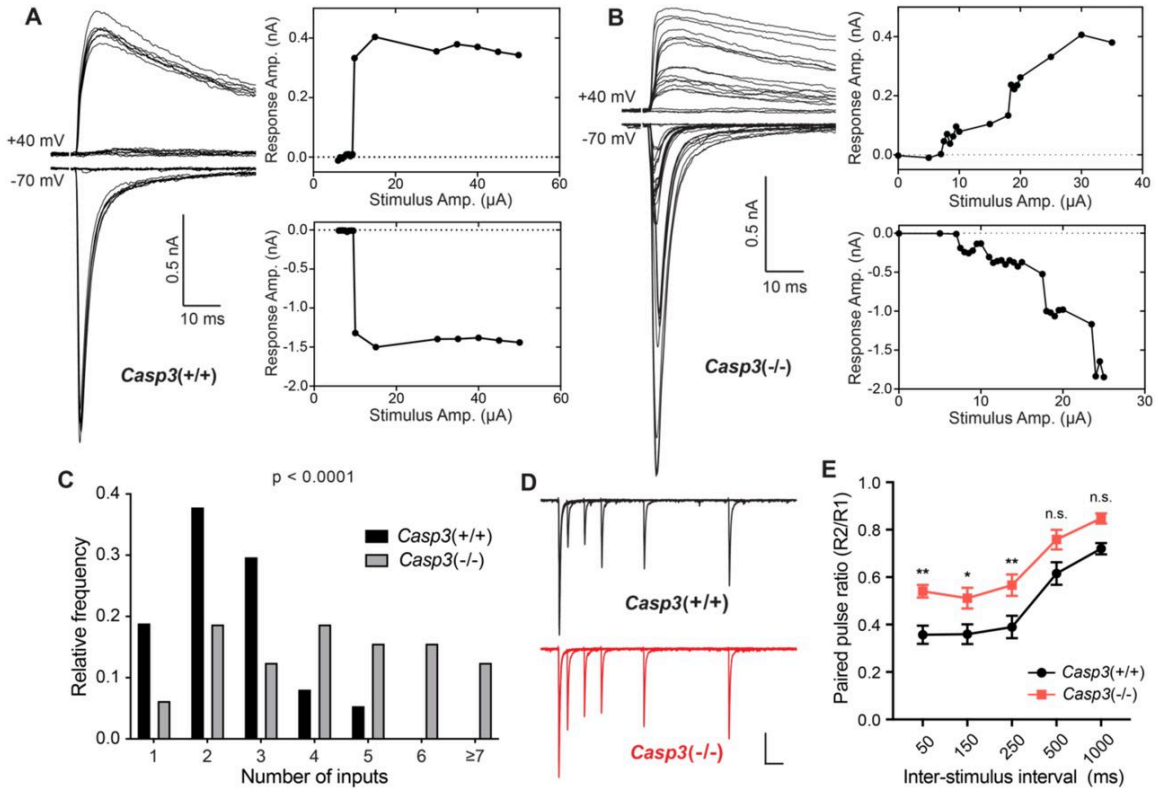


Figure 4. Caspase 3 is required for retinogeniculate circuit refinement. (**A-B**) Example recordings of dLGN relay neuron responses in P30 wildtype (**A**) and *Casp3*$^{-/-}$ (**B**) mice. Excitatory postsynaptic currents (EPSCs) were evoked by increasing stimulation currents in the optic tract. Both AMPAR-mediated inward current at -70 mV membrane potential and AMPAR and NMDAR-mediated outward current at +40 mV membrane potential are shown. Peak response amplitudes at each stimulation intensity are plotted to the right of recording traces. Scale bars represent 0.5 nA and 10 ms. (**C**) Distribution of RGC input numbers on individual dLGN relay neurons in wildtype and *Casp3*$^{-/-}$ mice. The number of RGC inputs was inferred by manually counting the number of steps in AMPAR-mediated EPSC response curves (lower right in **A**and **B**) while blind to the genotypes. P-value was calculated from two-tailed t-test. n=37 cells for wildtype mice and n=32 cells for *Casp3*$^{-/-}$ mice. (**D**) Example recordings from paired pulse measurements at -70 mV membrane potential in wildtype and *Casp3*$^{-/-}$mice. Traces from experiments with 50, 150, 250, 500, and 1000 ms inter-stimulus intervals are overlayed. Stimulus artifacts were removed from the traces for clarity. Scale-bars represent 100 ms (horizontal) and 0.3 nA (vertical). (**E**) Paired-pulse ratio (calculated as peak amplitude of the second response over that of the first response) in wildtype and *Casp3*$^{-/-}$ mice at various inter-stimulus intervals. Mean and standard error of the mean (SEM) are shown. P-values were calculated from Bonferroni's multiple comparison test. p=0.0067 for 50 ms interval, p=0.0369 for 150 ms interval, and p=0.0097 for 250 ms interval. n=16 cells for wildtype mice and n=13 for *Casp3*$^{-/-}$ mice.

doi.org/10.32388/TD1OXF

An increased number of RGC axons innervating dLGN relay neurons in *Casp3*$^{-/-}$ mice should correspond to greater numbers of presynaptic release sites. To infer the number of release sites, we stimulated the optic tract with a pair of stimuli in rapid succession and measured the paired-pulse response ratio (PPR) in dLGN relay neurons (**Fig. S7B** and **Fig. 4D-E**)[43][45]. In retinogeniculate synapses, the first stimulus significantly depletes the readily releasable pool (RRP) of neurotransmitters and reduces the response to the second stimulus, resulting in a small PPR (calculated as second response over first response) (**Fig. S7B**)[43][45]. If there is an increase in the number of release sites in *Casp3*$^{-/-}$ mice, we expect the RRP to expand, leading to a larger second response and PPR (**Fig. S7C**)[45]. Indeed, we found that the PPR was significantly greater in *Casp3*$^{-/-}$ dLGN relay neurons than in controls (**Fig. 4D-E**), suggesting that the inability to eliminate weak inputs resulted in an increase in the number of release sites from RGC inputs in *Casp3*$^{-/-}$ mice. Taken together, our results demonstrate that caspase-3 is required for experience-driven retinogeniculate circuit refinement. In the absence of caspase-3, weak RGC inputs cannot be eliminated, and dLGN relay neurons remain multiply innervated.

Microglia-mediated synapse elimination depends on caspase-3

Our results reveal activity-dependent caspase-3 activation at synapses as a key molecular event that directs synapse elimination in the retinogeniculate pathway but do not identify the cell types involved. Previous studies have demonstrated that both microglia and astrocytes participate in synapse elimination by engulfing synaptic material[7][10]. It is possible that caspase-3 activation at synapses might induce the display apoptosis-related cell surface markers that can be recognized by microglia and astrocytes for synapse elimination.

If microglia-mediated synapse elimination depends on caspase-3 activation, then microglia in *Casp3*$^{-/-}$ mice should engulf less synaptic material. Similar to a previous study[7], we utilized the *Cx3cr1-Gfp* transgenic mouse line to visualize microglia *in vivo.* In this line, a *Gfp*transgene is expressed under the control of the native *Cx3cr1* promoter to enable specific labeling of microglia in the brain (**Fig. 5A**)[46]. As a proxy for labeling retinogeniculate synapses, we labeled presynaptic RGC axon terminals by injecting *Casp3*$^{+/-}$; *Cx3cr1-Gfp*$^{+/-}$and *Casp3*$^{-/-}$; *Cx3cr1-Gfp*$^{+/-}$ littermate pups (*Casp3*$^{+/-}$ instead of *Casp3*$^{+/+}$ mice were used to enable more efficient breeding) at the age of P4 with fluorophore-conjugated CTB in the two eyes and harvested the brains at P5 (**Fig. 5A**)[7]. We used automatic segmentation to isolate volumes corresponding to microglia and RGC axon terminals (**Fig. 5B**) from regions in the dLGN where RGC inputs from both eyes were present (**Fig. 5A**). The presence of small soma and thin processes of microglia in

Casp3$^{-/-}$; *Cx3cr1-Gfp*$^{+/-}$ mice indicates that caspase-3 deficiency did not result in microglial activation (**Fig. 5B**), which is further validated by immunohistochemical analysis of microglia in caspase-3 deficient mice (**Fig. S9A-D**). To quantify synapse engulfment, we calculated the volume of labeled RGC terminals that were fully enclosed in each microglia (**Fig. 5C**). As expected, we observed that microglia in *Casp3*$^{-/-}$; *Cx3cr1-Gfp*$^{+/-}$ mice engulfed significantly less axonal material compared to those of *Casp3*$^{+/-}$; *Cx3cr1-Gfp*$^{+/-}$ littermates (**Fig. 5B-C**). The same trend was observed when RGC axon terminals originating from the two eyes were analyzed separately (**Fig. S10A-B**), suggesting that defects in microglia-mediated synapse engulfment in *Casp3*$^{-/-}$ mice affect inputs from both eyes. As the engulfment capacity of microglia is limited by their size, we normalized the volume of engulfed synaptic material in each microglia to the microglial volume (**Fig. 5D**). Microglia in both groups of mice are comparable in size (**Fig. S10C**), and the defect in synaptic engulfment observed in *Casp3*$^{-/-}$ mice persisted after normalization to microglial volume (**Fig. 5D**). Our results demonstrate that microglia-mediated synapse elimination depends on caspase-3.

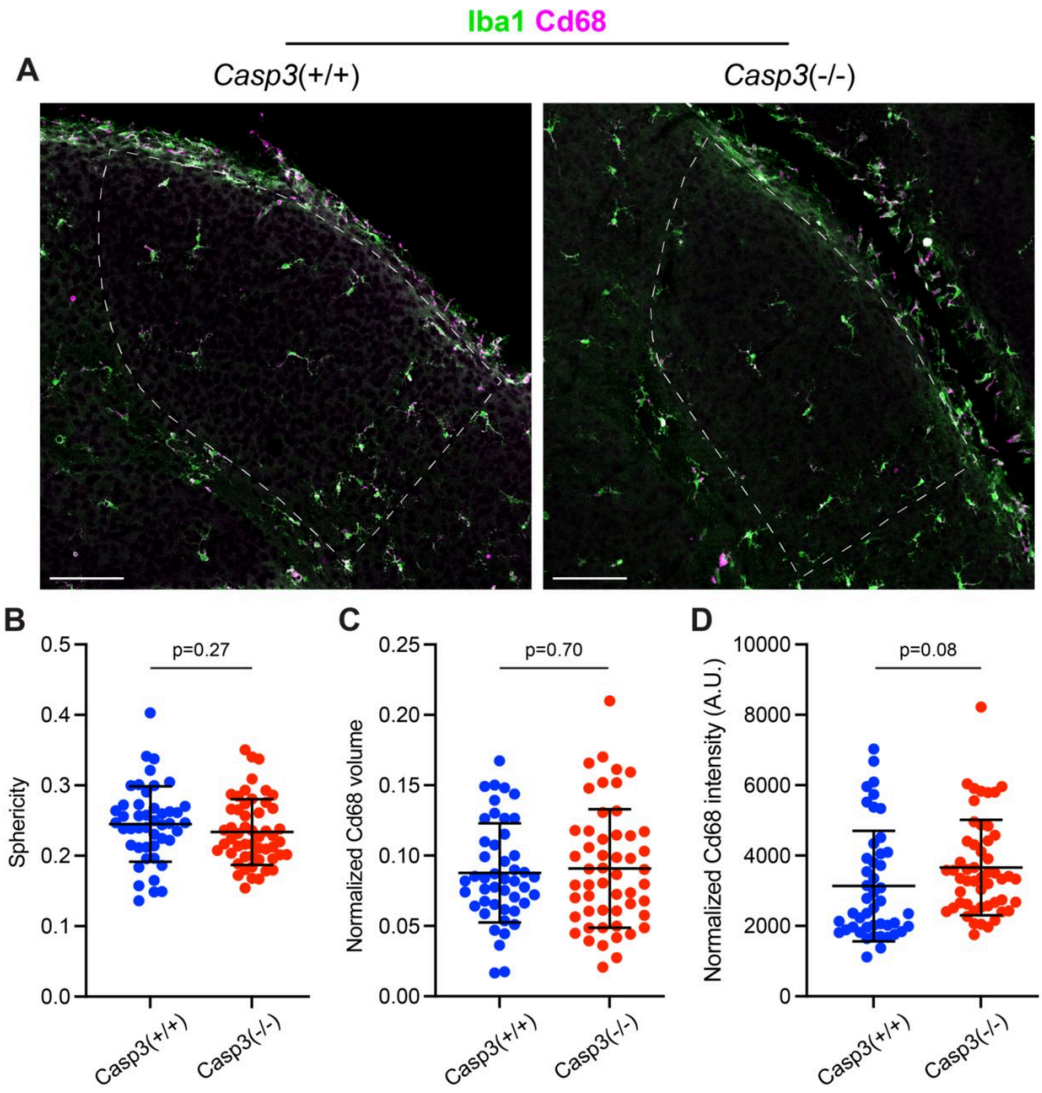


Figure S9. Caspase-3 deficiency does not cause microglia activation. (**A**) Representative images of P5 dLGNs in a *Casp3*$^{+/+}$ mouse (left) and a *Casp3*$^{-/-}$ mouse (right) showing Iba1 (green, a marker for microglia cell body) and Cd68 (magenta, a marker for microglia activation) staining. The dLGN areas are highlighted with dotted lines. Scale-bars represent 100 μm. (**B**) Quantification of microglia morphology in *Casp3*$^{+/+}$ and *Casp3*$^{-/-}$ mice using the sphericity metric. A sphericity of 1 corresponds to a perfect sphere. The smaller the sphericity is, the more ramified the cell is. (**C**-**D**) Quantification of microglia activation by normalizing the total volume of Cd68 signal (**C**) or the total intensity of Cd68 signal (**D**) in each microglia to the volume of that microglia. By both morphology and Cd68 signal, microglia in *Casp3*$^{-/-}$ mice show no evidence of activation. In **B**-**D**, each data point represents one microglia, and mean and S.D. are shown. n=46 microglia from 4 *Casp3*$^{+/+}$ mice and n=52 microglia from 4 *Casp3*$^{-/-}$ mice. P-values were calculated from two-tailed unpaired t-tests.

doi.org/10.32388/TD1OXF

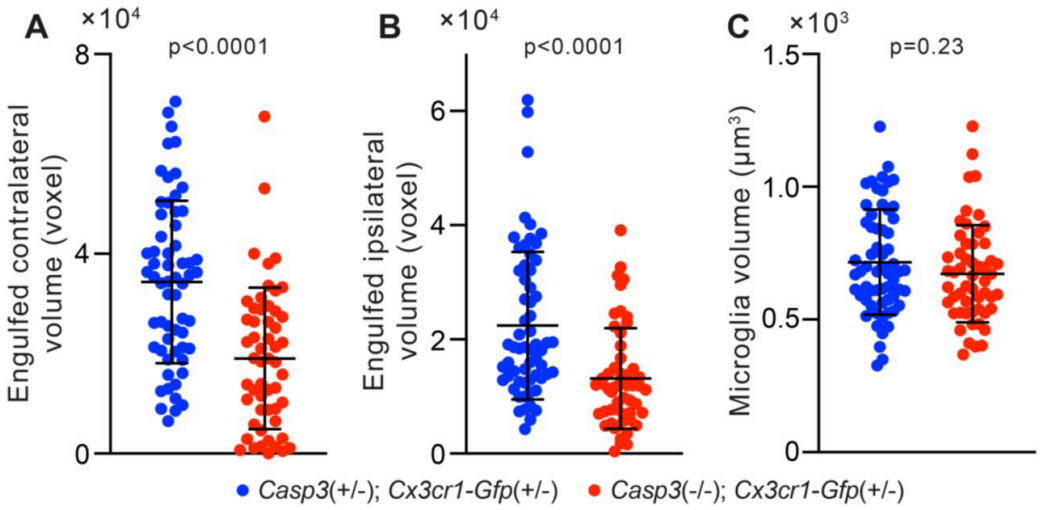


Figure S10. Additional analyses of microglia-mediated engulfment of synaptic material. (**A-B**) Volume of contralateral (**A**) and ipsilateral (**B**) RGC axon terminals engulfed by individual microglia in the P5 dLGN of *Casp3*$^{+/-}$; *Cx3cr1-Gfp*$^{+/-}$ and *Casp3*$^{-/-}$; *Cx3cr1-Gfp*$^{+/-}$ mice. (**C**) Volume of individual microglia in the P5 dLGN of *Casp3*$^{+/-}$; *Cx3cr1-Gfp*$^{+/-}$ and *Casp3*$^{-/-}$; *Cx3cr1-Gfp*$^{+/-}$ mice. In **A-C**, each point represents one microglia. Mean and S.D. are shown. P-values were calculated from unpaired two-tailed t-tests. n=61 microglia from 8 *Casp3*$^{+/-}$; *Cx3cr1-Gfp*$^{+/-}$ mice and n=54 microglia from 5 *Casp3*$^{-/-}$; *Cx3cr1-Gfp*$^{+/-}$ mice.

doi.org/10.32388/TD1OXF

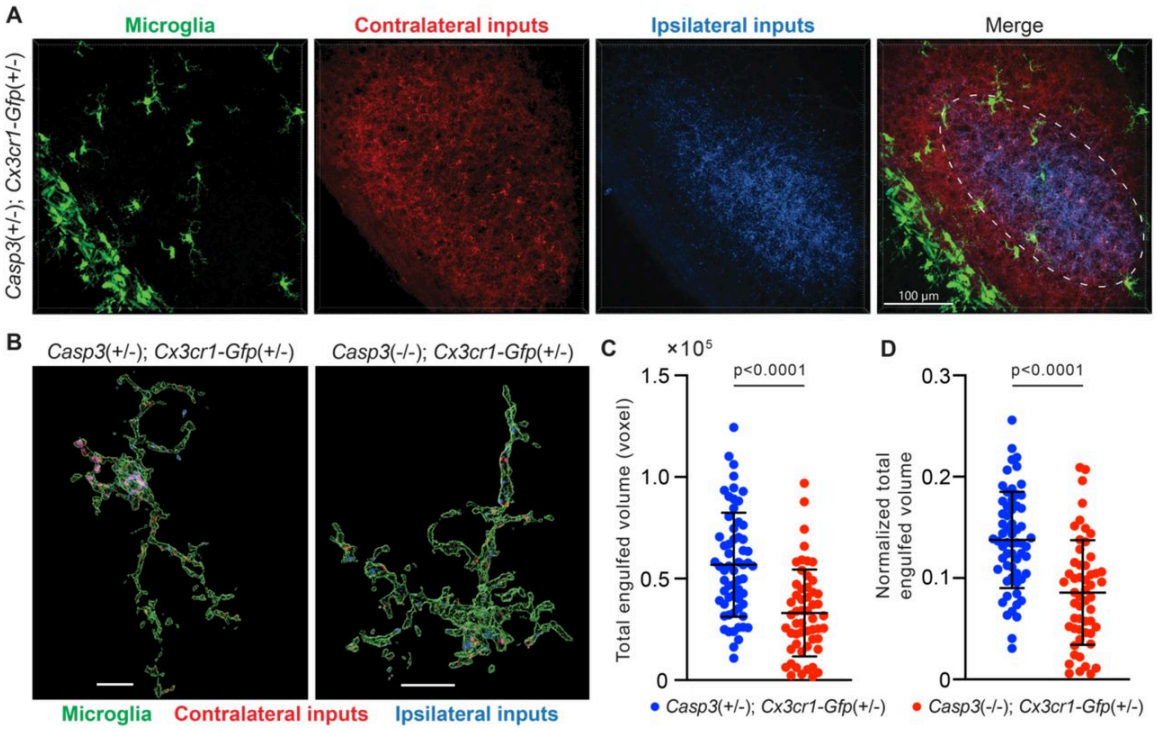


Figure 5. Microglia-mediated synapse elimination depends on caspase-3. (**A**) Representative 3D-reconstructed images of a P5 *Casp3*$^{+/-}$; *Cx3cr1-Gfp*$^{+/-}$ mouse dLGN with microglia displayed in green, contralateral RGC axon terminals in red, and ipsilateral RGC terminals in blue. In the merged image, the region from which microglia are selected for analysis is indicated with the dashed line. The scale-bar represents 100 μm. (**B**) Representative surface rendering of microglia (green) from P5 dLGNs of *Casp3*$^{+/-}$; *Cx3cr1-Gfp*$^{+/-}$ and *Casp3*$^{-/-}$; *Cx3cr1-Gfp*$^{+/-}$ mice. Intracellular contralateral (red) and ipsilateral (blue) RGC axon terminals are shown. Microglia from caspase-3 deficient mice engulf visibly less synaptic material. Scale-bars represent 10 μm. (**C**) Total volume of engulfed synaptic material in individual microglia from *Casp3*$^{+/-}$; *Cx3cr1-Gfp*$^{+/-}$ and *Casp3*$^{-/-}$; *Cx3cr1-Gfp*$^{+/-}$ mice. (**D**) Total volume of engulfed synaptic material in each microglia (from **C**) is normalized to the volume of that microglia. In **C**-**D**, each point represents one microglia. Mean and S.D. are shown. p-values were calculated from unpaired two-tailed t-tests. n=61 microglia from 8 *Casp3*$^{+/-}$; *Cx3cr1-Gfp*$^{+/-}$ mice and n=54 microglia from 5 *Casp3*$^{-/-}$; *Cx3cr1-Gfp*$^{+/-}$ mice.

Astrocytes utilize phagocytic receptors MerTK and Megf10 to eliminate synapses[10]. Both receptors have been implicated in the clearance of apoptotic cells[47][48]. We asked whether caspase-3 activation is also required for astrocyte-mediated synapse elimination. To visualize astrocytes, we used the *Aldh1l1-Gfp* transgenic mouse line, where a *Gfp* transgene under the control of the promoter of *Aldh1l1* is specifically expressed in astrocytes (**Fig. S11A**)[49]. We again labeled RGC axon terminals in *Casp3*$^{+/-}$; *Aldh1l1-Gfp*$^{+/-}$ and

Casp3$^{-/-}$; *Aldh1l1-Gfp*$^{+/-}$littermate mice with intraocular injection of CTB conjugates (**Fig. S11A**). Astrocytes were present in the P5 dLGN at a much higher density than microglia and possess very fine processes (**Fig. S11A**). To ensure segmentation fidelity, we only analyzed astrocyte cell bodies and their proximal processes (**Fig. S11B**). Unexpectedly, we found that the volume of axonal material engulfed by astrocytes was comparable in the two groups of mice (**Fig. S11C**). On average, astrocytes in caspase-3 deficient mice did engulf less axonal material (**Fig. S11C**), but the effect size appears too small to be biologically relevant, and the statistical significance was small considering that the sample size was large (**Fig. S11C**). The same trend was observed when we normalized the volume of engulfed synaptic material to astrocyte volume (**Fig. S11D-E**). It is possible that a more pronounced difference would be observed if *Casp3*$^{+/+}$mice were used for comparison. Nevertheless, the differential response to caspase-3 deficiency between microglia- and astrocyte-mediated synapse elimination raises the possibility that the two cell types may target distinct sets of synapses for elimination (see discussion).

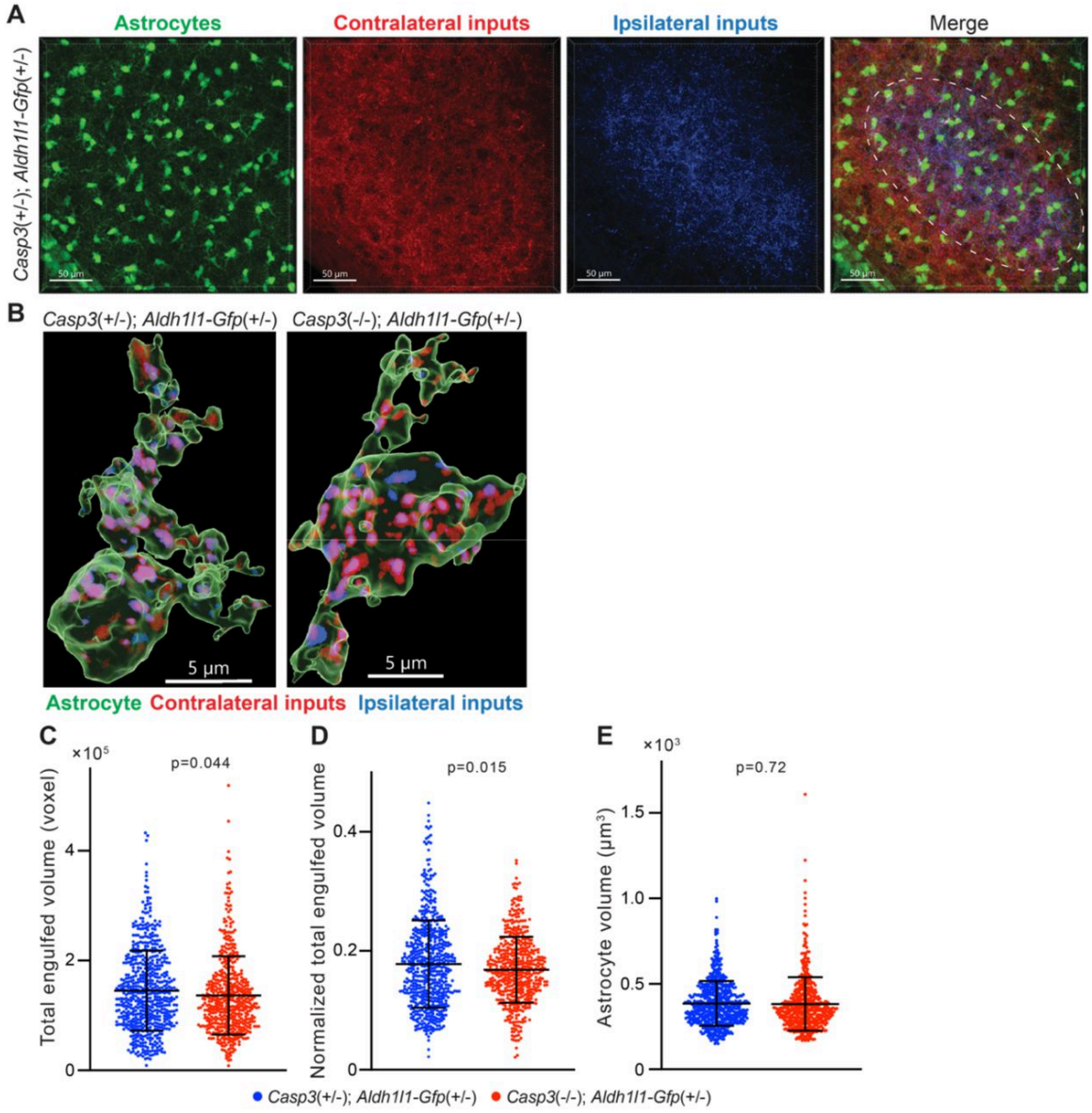


Figure S11. Astrocyte-mediated synapse elimination does not appear to depend on caspase-3. (**A**) Representative 3D-reconstructed images of a P5 *Casp3*$^{+/-}$; *Aldh1l1-Gfp*$^{+/-}$ mouse dLGN with astrocytes displayed in green, contralateral RGC axon terminals in red, and ipsilateral RGC terminals in blue. The region from which astrocytes are selected for analysis is indicated with the dashed line in the merged image. Scale-bars represent 50 μm. (**B**) Representative surface rendering of astrocytes (green) from P5 dLGNs of *Casp3*$^{+/-}$; *Aldh1l1-Gfp*$^{+/-}$ and *Casp3*$^{-/-}$; *Aldh1l1-Gfp*$^{+/-}$ mice. Intracellular contralateral (red) and ipsilateral (blue) RGC axon terminals are shown. Only cell bodies and the base of processes were segmented. We made this segmentation choice because we observed that fine astrocytic processes are largely devoid of engulfed material. Scale-bars represent 5 μm. (**C**) Total volume of engulfed synaptic material in individual astrocytes from *Casp3*$^{+/-}$; *Aldh1l1-Gfp*$^{+/-}$ and *Casp3*$^{-/-}$; *Aldh1l1-Gfp*$^{+/-}$ mice. (**D**) Total volume of engulfed synaptic material in each astrocyte (from **C**) is normalized to the volume of that astrocytes. (**E**) Volume of individual astrocytes from the two groups of mice. In **C**–**E**, each

doi.org/10.32388/TD1OXF

point represents one astrocyte. Mean and S.D. are shown. P-values were calculated from unpaired two-tailed t-tests. n=595 astrocytes from 8 *Casp3*$^{+/-}$; *Aldh1l1-Gfp*$^{+/-}$ mice and n=517 astrocytes from 6 *Casp3*$^{-/-}$; *Aldh1l1-Gfp*$^{+/-}$ mice.

Caspase-3 activation determines synapse elimination specificity

Our data demonstrate that caspase-3 is activated at weak/inactive synapses, and that microglia eliminate less synaptic material when caspase-3 activation is blocked. Combining the two observations, we hypothesize that activity-dependent caspase-3 activation at synapses is a key molecular event that directs microglia to specifically eliminate weaker synapses. This model predicts that in caspase-3 deficient mice, microglia should lose the ability to preferentially target weaker synapses.

To test this model, we inactivated retinogeniculate synapses originating from right eyes in *Casp3*$^{+/+}$ and *Casp3*$^{-/-}$ mice with AAV-hSyn-TeTxLC injections (**Fig. 6A**). A group of control animals was included for each genotype that received AAV-hSyn-Turq injections. We then labeled RGC axon terminals from both eyes with CTB conjugates in all animals and analyzed microglia-mediated synapse engulfment (**Fig. 6B-G**). According to our model, in TeTxLC-injected *Casp3*$^{+/+}$ mice, microglia should preferentially engulf inactive retinogeniculate synapses originating from the right eye (**Fig. 6A**), whereas in TeTxLC-injected *Casp3*$^{-/-}$ mice, synapses from the right and the left eye should be engulfed at similar levels regardless of their strength (**Fig. 6A**). To quantitatively detect preferential synapse engulfment by microglia, a comparison between TeTxLC-injected and control-injected animals is necessary (**Fig. 6B, C**, and **F**). We first calculated the ratio between the volume of right eye-originated RGC axon terminals and left eye-originated terminals that were engulfed by each microglia. Then, by comparing this right-to-left engulfment ratio computed in TeTxLC-injected and control-injected animals, preferential engulfment of inactivated synapses from right eyes could be detected as higher engulfment ratios in TeTxLC-injected animals (**Fig. 6F**). It is worth noting that microglia-related confounding factors, such as possible alterations in microglia physiology due to caspase-3 deficiency or surgical manipulations, cancel out when calculating engulfment ratios, allowing information pertaining only to substrate preference to be isolated.

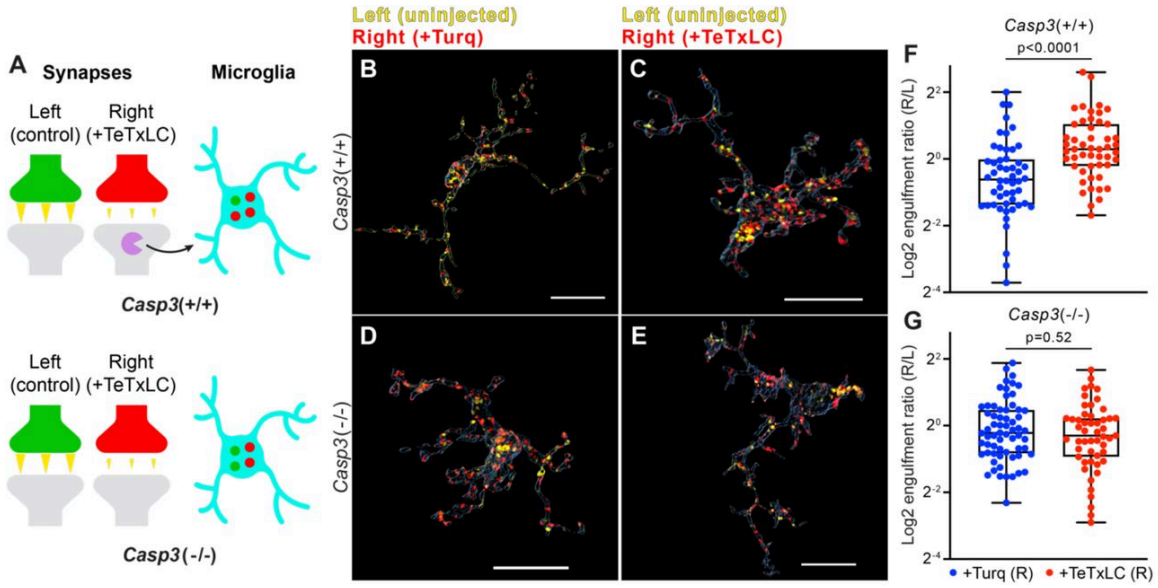


Figure 6. Caspase-3 activation determines specificity of microglia-mediated synapse elimination. (**A**) Schematics illustrating the experimental rationale. In wildtype mice (upper panel), inactivating retinogeniculate synapses from the right eye activates caspase-3 (magenta pie) and recruits microglia to engulf more right eye-originated synapses (red dots) than left eye-originated synapses (green dots). If caspase-3 activation is blocked (lower panel), we expect preferential engulfment of inactive synapses to be attenuated. (**B-E**) Surface rendering of representative microglia from P5 left dLGN of *Casp3*$^{+/+}$ (**B-C**) or *Casp3*$^{-/-}$ (**D-E**) mice injected with AAV expressing mTurquoise2 (**B** and **D**) or TeTxLC (**C** and **E**) in the right eye at E15. RGC axon terminals from the left eye are shown in yellow and terminals from the right eye in red. Scale bars represent 15 μm. (**F-G**) Ratio between volumes of right-eye and left-eye-originated synaptic material engulfed by microglia from *Casp3*$^{+/+}$ (**F**) or *Casp3*$^{-/-}$(**G**) mice injected with AAV expressing mTurquoise2 (blue) or TeTxLC (red). Each dot represents one microglia. Engulfment ratios are displayed on a log scale. 0, 25, 50, 75, and 100 percentiles are shown. p-values were calculated from unpaired two-tailed Mann-Whitney tests. n=52 microglia from 7 Turq-injected *Casp3*$^{+/+}$ mice, n=50 microglia from 8 TeTxLC-injected *Casp3*$^{+/+}$ mice, n=64 microglia from 5 Turq-injected *Casp3*$^{-/-}$ mice, and n=51 microglia from 6 TeTxLC-injected *Casp3*$^{-/-}$ mice.

Consistent with previous studies[7], in *Casp3*$^{+/+}$ mice inactivation of retinogeniculate synapses from the right eye led to enhanced microglia-mediated engulfment of right eye-originated RGC axon terminals but not left eye-originated terminals (**Fig. S12A-B**), resulting in a significant increase in right-to-left engulfment ratios in microglia of TeTxLC-injected animals compared to control-injected animals (**Fig. 6B, C**, and **F**). In contrast, engulfment ratios were similar between TeTxLC-injected and control-injected *Casp3*$^{-/-}$ mice (**Fig. 6D, E** and **G** and **Fig. S12C-D**), suggesting that microglia could no longer distinguish

doi.org/10.32388/TD1OXF

between strong and weak synapses in the absence of caspase-3 activation. Summing the evidence obtained thus far, we propose the activity-dependent caspase-3 activation is a crucial signaling event that integrates upstream information about synaptic activity, takes place at weak/inactive synapses, and recruits downstream microglia to eliminate synapses in an activity-dependent manner.

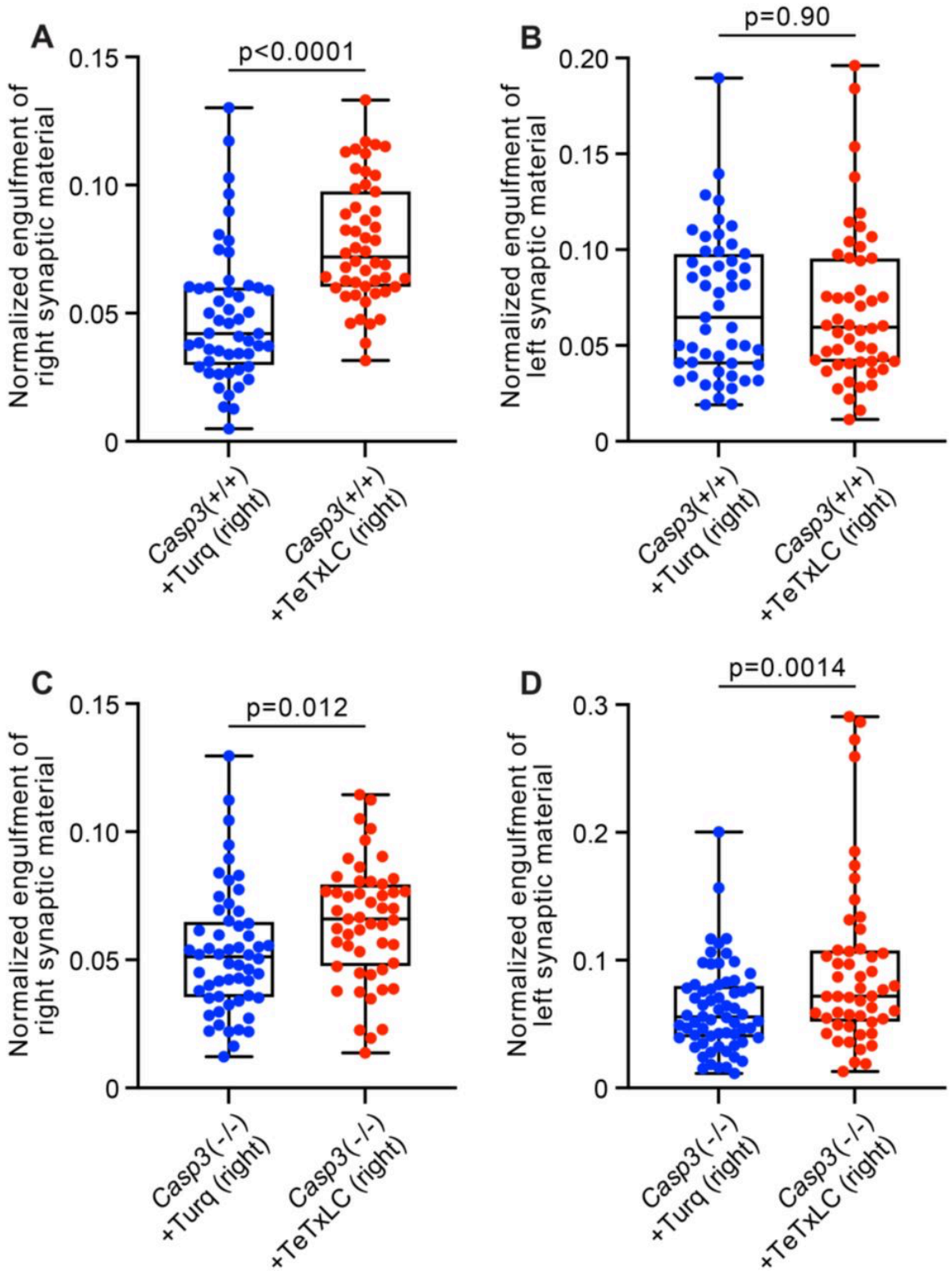


Figure S12. Additional analysis on activity-dependent microglia-mediated engulfment of synapses. (**A**-**D**) Volumes of synaptic material originating from right (**A** and **C**) or left (**B** and **D**) eyes engulfed by individual microglia from the left dLGN of *Casp3*$^{+/+}$ (**A**-**B**) or *Casp3*$^{-/-}$ (**C**-**D**) mice injected with AAV expressing

doi.org/10.32388/TD1OXF

mTurquoise2 (blue) or TeTxLC (red) in right eye were normalized to microglial volume and plotted. In *Casp3*$^{+/+}$ mice, inactivating right eye-originated retinogeniculate synapses specifically enhanced microglia-mediated engulfment of RGC axon terminals from right eyes (**A**) but not left eyes (**B**), resulting in significantly higher engulfment ratios (**Fig. 6F**). In *Casp3*$^{-/-}$ mice, inactivating right eye-originated synapses upregulated engulfment of RGC terminals from both eyes (**C** and **D**), resulting in no significant change in engulfment ratios (**Fig. 6G**). In **A**-**D**, 0, 25, 50, 75, and 100 percentiles are shown. p-values were calculated from unpaired two-tailed t-tests. n=52 microglia from 7 Turq-injected *Casp3*$^{+/+}$ mice, n=50 microglia from 8 TeTxLC-injected *Casp3*$^{+/+}$ mice, n=64 microglia from 5 Turq-injected *Casp3*$^{-/-}$ mice, and n=51 microglia from 6 TeTxLC-injected *Casp3*$^{-/-}$ mice. ***Notes on interpretation of C and D***:We observed that in *Casp3*$^{-/-}$ brains, particularly those injected with TeTxLC, microglia in dLGNs tended to increase in volume and have thicker processes. We therefore suspect the non-specific upregulation of synapse engulfment in TeTxLC-injected *Casp3*$^{-/-}$ mice is a consequence of microglial activation rather than synapse inactivation. This microglial activation is likely a ramification of intraocular surgeries, as changes in microglia morphology was more prominent in the left dLGN that received most of the inputs from AAV-injected right eyes, and microglia outside of dLGNs did not show characteristics of activation. We noticed that *Casp3*$^{-/-}$ brains tended to have weak structural integrity. It is likely that repetitive intraocular injections caused damage in the retinogeniculate pathway of *Casp3*$^{-/-}$ mice and activated microglia. Nevertheless, by calculating right-to-left engulfment ratios, substrate preference of microglia in TeTxLC-injected *Casp3*$^{-/-}$ mice can be deduced.

Caspase-3 deficiency protects against amyloid-β-induced synapse loss

Lastly, we wanted to test if caspase-3 regulates synapse loss in neurodegenerative diseases through mechanisms analogous to its role in activity-dependent synapse elimination. To this end, we focused on Alzheimer's disease (AD). AD is the most common cause of dementia[50], and synapse loss is the strongest correlate of cognitive decline in AD patients[51]. Accumulation and deposition of oligomeric or fibril amyloid-β (Aβ) peptide has been proposed to be the cause of neurodegeneration in AD[50]. Intriguingly, oligomeric Aβ impairs long-term potentiation (LTP)[52], and this suppression of LTP requires caspase-3 activation[53]. Additionally, caspase-3 activation has been linked to early synaptic dysfunction in an AD mouse model[54].

To test if synapse loss in AD requires caspase-3, we utilized the APP/PS1 mouse line, in which amyloid precursor protein (APP) and presenilin 1 (PS1) carrying mutations associated with early-onset familial AD are overexpressed in CNS neurons[55]. We observed that female *App/Ps1*$^{+/-}$ mice developed amyloid deposits in the hippocampus and cortex by 5 months (**Fig. S13Aii**), and the amyloid burden worsened by 6

months (**Fig. S13Aiii**). In male *App/Ps1*$^{+/-}$mice, amyloid deposits only became apparent at 6 months and occurred at a lower level compared to age-matched females (**Fig. S13Aiv-v**). We focused on analyzing *App/Ps1*$^{+/-}$female mice in subsequent experiments to obtain robust phenotypes. To quantify synapse loss, we labeled presynaptic and postsynaptic compartments in the dentate gyrus of 6 month-old *App/Ps1*$^{-/-}$ and *App/Ps1*$^{+/-}$ littermates by detecting synaptic vesicle protein 2 (SV2) and Homer1, respectively, and selected multiple fields of interest per animal for imaging analysis while avoiding regions adjacent to amyloid deposits (**Fig. S14**). We fitted ellipsoids to SV2 and Homer1 signals to identify pre- and post-synaptic puncta and defined synapses as Homer1-SV2 punctum pairs that were less than 300 nm apart (**Fig. 7A**). We observed that synapse density in *App/Ps1*$^{+/-}$ mice was significantly reduced compared to that in *App/Ps1*$^{-/-}$ littermate controls (**Fig. 7A-B**), and that this reduction could be attributed to lower densities of both pre- and post-synaptic puncta in *App/Ps1*$^{+/-}$ mice (**Fig. S15A-B**). We then crossed APP/PS1 mice to caspase-3 deficient mice and quantified synapse density in 6 month-old *Casp3*$^{-/-}$; *App/Ps1*$^{-/-}$ and *Casp3*$^{-/-}$; *App/Ps1*$^{+/-}$ littermate mice (**Fig. S14**). We observed that, in the caspase-3 deficient background, overexpression of mutant APP and PS1 no longer resulted in a reduction in the density of synapses (**Fig. 7C-D**) or pre-/post-synaptic puncta (**Fig. S15C-D**), suggesting that caspase-3 activity is required for Aβ-induced synapse loss in the APP/PS1 mouse model. Intriguingly, levels of amyloid deposition were comparable between *App/Ps1*$^{+/-}$ and *Casp3*$^{-/-}$; *App/Ps1*$^{+/-}$ mice (**Fig. S13Avi** and **B**), and reactive microglia were observed near amyloid deposits regardless of caspase-3 deficiency (**Fig. S16**), indicating that protection conferred by caspase-3 deficiency against Aβ-induced synapse loss might not require inhibition of amyloid accumulation or microgliosis. We also investigated whether Aβ accumulation induced elevated levels of caspase-3 activity. We analyzed 4, 5, and 6 month-old *App/Ps1*$^{-/-}$ and *App/Ps1*$^{+/-}$mice but only observed robust upregulation of caspase-3 activity in the dentate gyrus of a subset of 4 month-old *App/Ps1*$^{+/-}$ mice (**Fig. S17A-C**). Upregulated caspase-3 activity in these mice remained in a punctate pattern without inducing neuronal death (**Fig. S17D-F**). It is possible that Aβ transiently induces caspase-3 activation in *App/Ps1*$^{+/-}$ mice, but stochasticity in the onset and duration of such induction prevents reliable detection with our sample size and temporal resolution. Overall, our results demonstrate caspase-3 as an important regulator of Aβ-induced synapse loss and a potential therapeutic target for AD treatment.

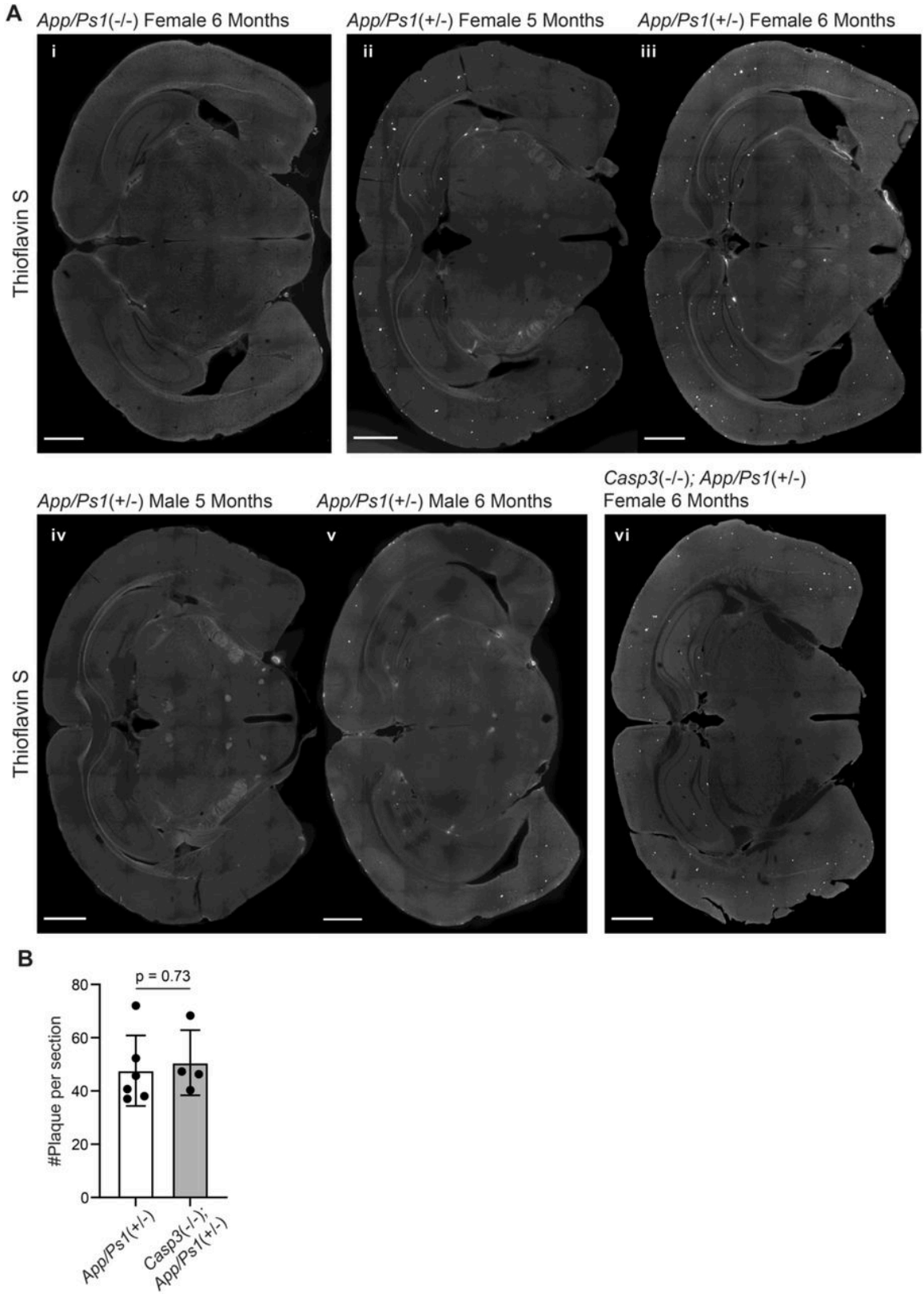


Figure S13. Amyloid deposition APP/PS1 mouse lines. (**A**) Images of coronal brain sections of a female *App/Ps1*$^{-/-}$ mouse at 6 months (i), female *App/Ps1*$^{+/-}$ mice at 5 months (ii) or 6 months (iii), male *App/Ps1*$^{+/-}$ mice at 5

doi.org/10.32388/TD1OXF

months (iv) or 6 months (v), and a female *Casp3*$^{-/-}$; *App/Ps1*$^{+/-}$ mouse at 6 months, stained with Thioflavin S to reveal Aβ plaques (bright spots in hippocampus and cortex). Scale-bars represent 1 mm. (**B**) Quantification of the number of plaques per section in female 6 month-old *App/Ps1*$^{+/-}$ and *Casp3*$^{-/-}$; *App/Ps1*$^{+/-}$ mice. Mean and S.D. are shown. p-values were calculated with unpaired two-tailed t-tests. n=6 for *App/Ps1*$^{+/-}$ mice and n=4 for *Casp3*$^{-/-}$; *App/Ps1*$^{+/-}$ mice.

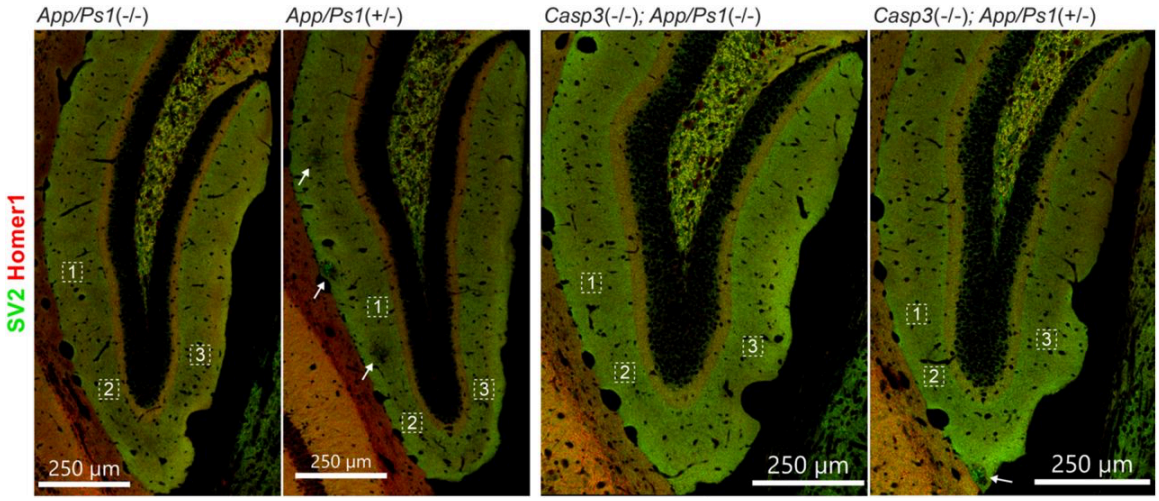


Figure S14. Selection of field of interest for synapse loss analysis. To quantify synapse density, three regions of interest from each dentate gyrus on either side of the brain were chosen for each animal (total of 6 regions per animal). Regions of interest in one dentate gyrus of one animal from each genotype group are highlighted with dotted squares in the overviews above. High resolution images of SV2 (in green) and Homer1 (in red) stains were acquired for each region of interest and used for analysis. In sections from animals overexpressing mutant APP and PS1, we avoided choosing regions of interest from areas surrounding amyloid plaques (highlighted with arrows).

doi.org/10.32388/TD1OXF

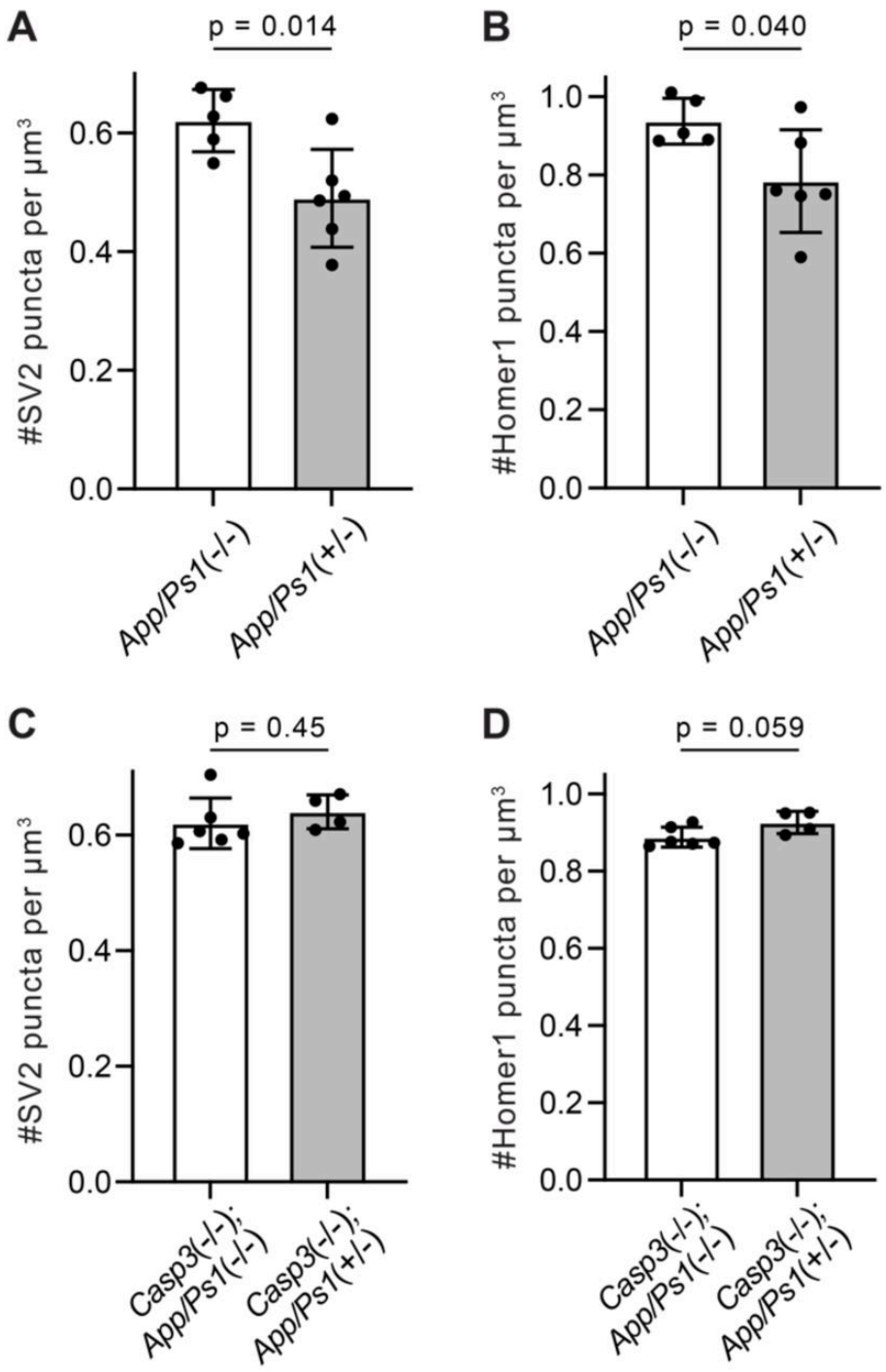


Figure S15. Additional analysis of synapse density in APP/PS1 mouse lines. (**A**-**D**) Quantification of presynaptic (**A** and **C**) and postsynaptic (**B** and **D**) puncta densities in the dentate gyrus of APP/PS1 mice in the caspase-3 wildtype (**A** and **B**) or deficient (**C** and **D**) background. Mean and S.D. are shown. p-values were calculated from unpaired two-tailed t-tests. n=5 for *App/Ps1*$^{-/-}$ mice, n=6 for *App/Ps1*$^{+/-}$ mice, n=6 for *Casp3*$^{-/-}$; *App/Ps1*$^{-/-}$ mice, and n=4 for *Casp3*$^{-/-}$; *App/Ps1*$^{+/-}$ mice.

doi.org/10.32388/TD1OXF

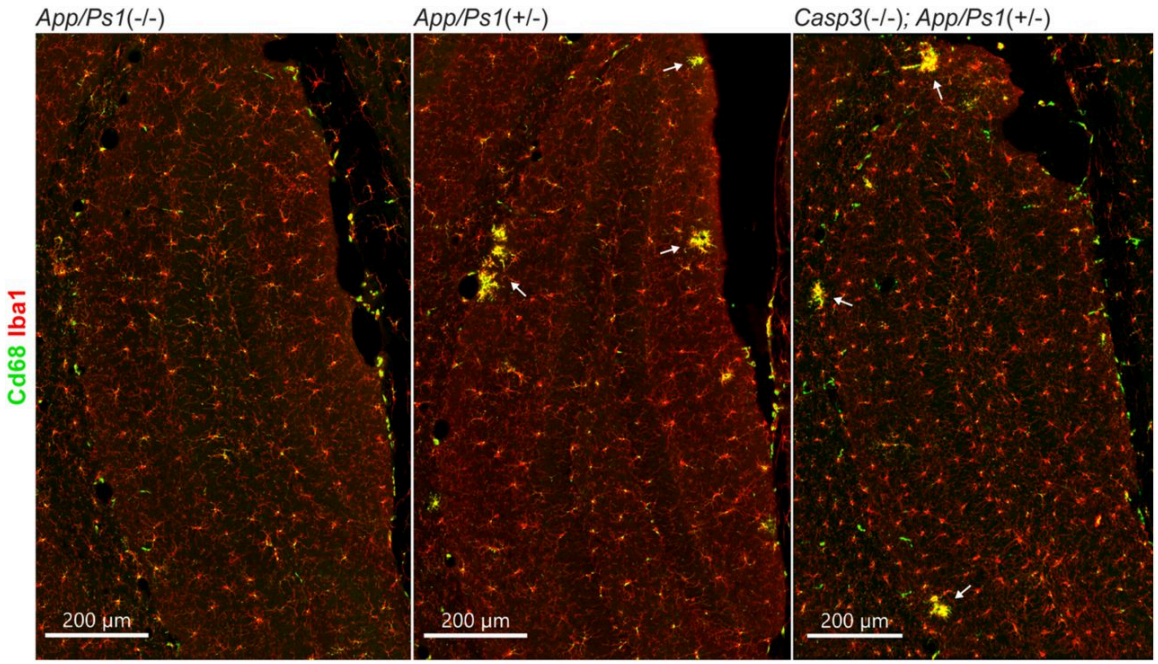


Figure S16. Microgliosis in APP/PS1 mouse lines. Coronal sections from 6 month-old female *App/Ps1*$^{-/-}$ (left), *App/Ps1*$^{+/-}$ (middle), and *Casp3*$^{-/-}$; *App/Ps1*$^{+/-}$ (right) mice were stained for Iba1 (red, to detect microglia) and Cd68 (green, as a microglia activation marker). Dentate gyrus regions are shown in the overviews above. Clusters of reactive microglia surrounding amyloid plaques are highlighted with arrows.

doi.org/10.32388/TD1OXF

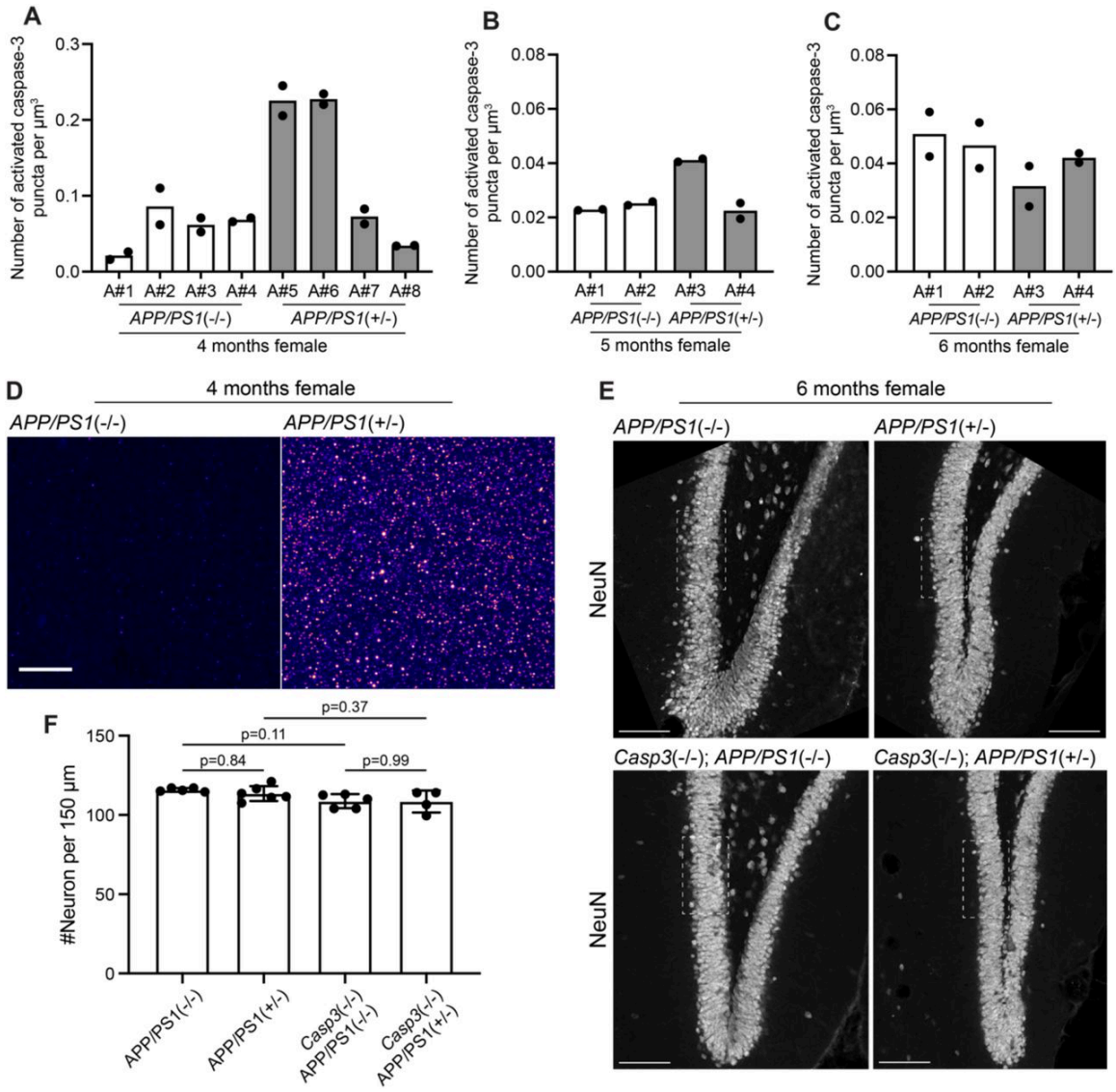


Figure S17. Aβ-induced caspase-3 activity in APP/PS1 mice. (**A**-**C**) Density of activated caspase-3 puncti in the dentate gyrus of 4 month-old (**A**), 5 month-old (**B**), and 6 month-old (**C**) female *App/Ps1*$^{-/-}$ and *App/Ps1*$^{+/-}$ mice. Each column represents one animal, and each dot represent quantification from one dentate gyrus (either from left side or right side). Two out of four 4-month-old *App/Ps1*$^{+/-}$ mice showed robustly upregulation of caspase-3 activity in the dentate gyrus (**A**). No upregulation of caspase-3 activity was observed in 5 month-old or 6 month-old mice. (**D**) Images showing elevated caspase-3 activity in the molecular layer of the dentate gyrus of a 4 month-old female *App/Ps1*$^{+/-}$ mouse (A#5 in **A**). Images were set to the same intensity contrast. Upregulated caspase-3 activity remained in a punctate pattern and no apoptotic cell was observed. Scale-bar represents 10 μm. (**E**) Representative images of the dentate gyrus in 6 month-old female *App/Ps1*$^{-/-}$, *App/Ps1*$^{+/-}$, *Casp3*$^{-/-}$; *App/Ps1*$^{-/-}$, and *Casp3*$^{-/-}$; *App/Ps1*$^{+/-}$ mice that were stained with an anti-NeuN antibody to visualize neurons. The fields of interest used to quantify neuron density are highlighted with dotted rectangles. Scale-bars represent 100 μm. (**F**) Neuron density in the granule cell layer of the dentate gyrus in the four groups of mice

doi.org/10.32388/TD1OXF

shown in **E**. Neither caspase-3 deficiency nor APP/PS1 overexpression caused significant changes in neuron density. Mean and S.D. are shown. p-values were calculated from Tukey's multiple comparisons test. n=5 for *App/Ps1*$^{-/-}$ mice, n=6 for *App/Ps1*$^{+/-}$ mice, n=5 for *Casp3*$^{-/-}$; *App/Ps1*$^{-/-}$ mice, and n=4 for *Casp3*$^{-/-}$; *App/Ps1*$^{+/-}$ mice.

doi.org/10.32388/TD1OXF

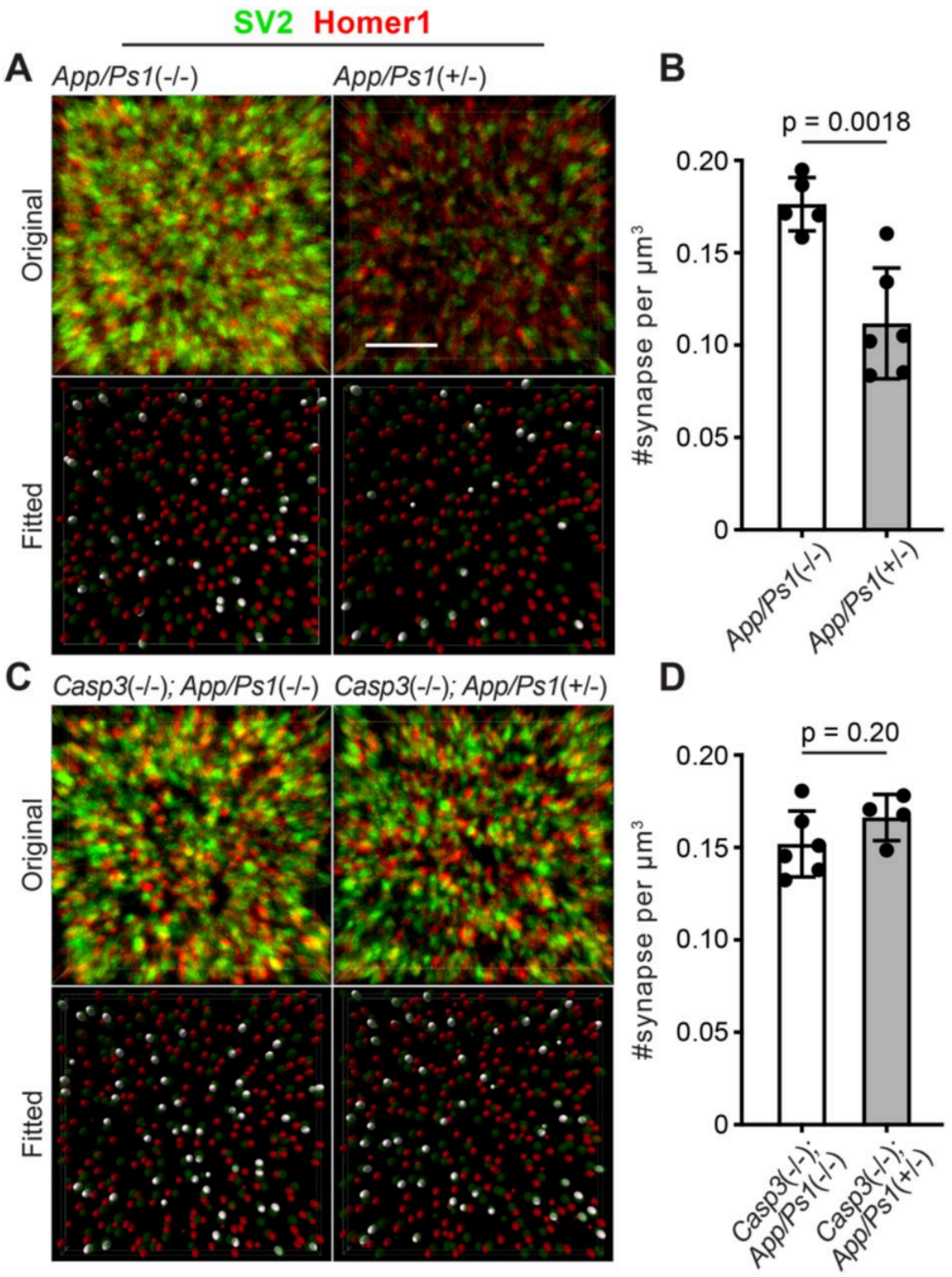


Figure 7. Caspase-3 deficiency protects against Aβ induced synapse loss. (**A** and **C**) Representative 3D-reconstructed images (3 μm in z) showing presynaptic (SV2, in green) and postsynaptic (Homer1, in red) signals in dentate gyrus of female 6 month-old APP/PS1 mice on caspase-3 wildtype (**A**) and deficient (**C**) backgrounds. Ellipsoids were fitted to the original images (upper panels) to isolate pre- (green) and post-synaptic (red) puncta

doi.org/10.32388/TD1OXF

(lower panels). Homer1 ellipsoids found with 300 nm of a SV2 ellipsoid are highlighted in white in the fitted images. Original images are adjusted to the same contrast. For the fitted images, only ellipsoids from the upper half of the z-stack are shown. Scale-bar represents 4 μm. (**B** and **D**) Quantification of synapse density in APP/PS1 mice on caspase-3 wildtype (**B**) and deficient (**D**) backgrounds. Mean and S.D. are shown. p-values were calculated from unpaired two-tailed t-tests. n=5 for *App/Ps1*$^{-/-}$ mice, n=6 for *App/Ps1*$^{+/-}$mice, n=6 for *Casp3*$^{-/-}$; *App/Ps1*$^{-/-}$ mice, and n=4 for *Casp3*$^{-/-}$; *App/Ps1*$^{+/-}$ mice.

Discussion

A model for caspase-3 dependent synapse elimination

Our findings support a model where competition between strong/active synapses and weak/inactive synapses in the retinogeniculate pathway triggers caspase-3 activation in the postsynaptic compartments of weaker synapses. This activation signals microglia to selectively eliminate these weaker synaptic connections, thereby facilitating the establishment of mature circuits in the visual pathway.

Mechanisms of activity-dependent caspase-3 activation

In the experiment where we demonstrated activity-dependent caspase-3 activation, we inactivated all retinogeniculate synapses from one eye to induce sufficiently high caspase-3 activity that can be discerned from background. It is important to note that this degree of inactivation is not typical for normal development. Consequently, caspase-3 activation in entire dLGN relay neurons observed in this experimental setting should not be interpreted as a physiological outcome of activity-dependent synapse elimination. In fact, apoptotic neurons were infrequently observed in the dLGN of control animals (**Fig. 1D** and **2B**), suggesting that during normal development, activity-dependent caspase-3 activation is predominantly localized and generally does not lead to neuronal death. Previous studies have proposed ubiquitin-dependent proteasomal degradation as a mechanism that can restrain caspase-3 activity to local sites in dendrites[24][56][57].

Intriguingly, synaptic inactivation in our experiment was achieved through TeTxLC expression in presynaptic RGCs, but caspase-3 activation was observed in postsynaptic relay neurons. Conversely, while caspase-3 is activated in the postsynaptic compartment, we were able to detect defects in synapse elimination using assays that measure presynaptic inputs. These observations suggest that activity-dependent caspase-3 activation requires synaptic transmission, and that caspase-3 dependent synapse

elimination is not strictly axonal or dendritic but involves both pre- and post-synaptic compartments. An important limitation of this study is that experiments in full-body *Casp3*$^{-/-}$ mice cannot query the roles of caspase-3 in presynaptic and postsynaptic compartments separately. Future experiments that perturb caspase-3 activation and other signaling events specifically in the pre- or post-synaptic compartments are needed to reveal more detailed mechanisms of activity-dependent synapse elimination.

The observation that activity-dependent caspase-3 activation requires synaptic competition resonates with previous research demonstrating that relative synaptic efficacy biases the outcome of synapse elimination during development of neuromuscular junctions and the callosal pathway[15][33][58][59]. However, the mechanisms linking synaptic competition with caspase-3 activation remains elusive. During LTD, caspase-3 is activated through mitochondrial release of cytochrome-c[18]. Whether synaptic competition could induce caspase-3 activation via mechanisms such as calcium signaling, which regulates both neurotransmission and cytochrome-c release[60], is an outstanding question.

Roles of microglia and astrocytes in synapse elimination

The differential impact of caspase-3 deficiency on microglia- and astrocyte-mediated synapses elimination in the visual pathway suggest that the two glial cell types have nonidentical substrate specificities when engulfing synaptic material. Indeed, considering that astrocytes are present at nearly ten-fold greater density than microglia in the developing dLGN (**Fig. 5A** and **S11A**) and have comparable engulfing capacities (**Fig. 5D** and **S11D**), contribution from microglia in synapse elimination would be negligible if the two cell types target the same substrates, which contradicts previous findings[7][14]. A recent study discovered that during clearance of apoptotic neurons in adult brains, microglia engulf the soma and proximal dendrites while astrocytes target distal dendrites, and this difference in substrate preference is at least partially attributed to differential kinetics in binding and engulfing substrates by the two cell types[61]. Investigating whether a similar division-of-labor exists during development could provide critical insights into the mechanisms of activity-dependent, glia-mediated synapse elimination.

It is often assumed in the literature that microglia directly engulf intact synapses, but existing data also support an alternative model where microglia indirectly contribute to synapse elimination by engulfing synaptic debris that is shed through neuron-autonomous mechanisms[62]. The observation that synaptic activity instructs microglial engulfment through caspase-3 activation raises the possibility that weakened synapses partially disintegrate through apoptosis-like mechanisms prior to being engulfed by microglia.

Further studies are needed to elucidate the intermediate steps between caspase-3 activation and microglial engulfment of synapses.

Molecular link between caspase-3 activation and microglial engulfment

How does caspase-3 activation at synapses recruit microglia for engulfment? Caspase-3 activation is known to trigger the display of apoptosis markers that can be recognized by phagocytes[19]. One of the best understood markers is phosphatidylserine (PtdSer), a phospholipid that translocates from the cytoplasmic leaflet of the plasma membrane to the exoplasmic leaflet during apoptosis[19]. Importantly, caspase-3 directly regulates the enzymes that translocate PtdSer through enzymatic cleavage[63][64]. Two recent studies demonstrated that PtdSer is displayed on retinogeniculate synapses during postnatal development, and microglia use the exposed PtdSer as a cue to target and engulf synapses[8][9]. Whether PtdSer exposure is upregulated in response to synapse weakening and whether caspase-3 activity is required for such exposure are important questions that require further investigation.

The complement protein C1q has been observed to bind to PtdSer on apoptotic cells and facilitate phagocytic clearance[19]. Additionally, a previous study found caspase-3 activity in C1q-bound synaptosomes[65], suggesting that C1q may bridge caspase-3 activation and synapse elimination. However, we investigated C1q expression and localization in the dLGN of P5 TeTxLC-injected mice but did not observe upregulation of C1q abundance or colocalization between C1q and caspase-3 activity (data not shown).

Caspase-3 as a potential target for AD treatment

Our findings suggest that caspase-3 deficiency confers protection against Aβ-induced synapse loss in a mouse model of AD. Notably, the absence of caspase-3 does not seem to affect Aβ deposition or microglia reactivity, indicating that caspase-3 depletion may mitigate synapse loss by directly countering Aβ-induced synaptic toxicity. Given the prominence of Aβ and inflammation as targets for AD drug development[66], inhibiting caspase-3 activity offers a potential alternative therapeutic strategy that could complement and enhance current treatment approaches. Therefore, it is important to test whether pharmacological inhibition of caspase-3 can effectively slow synapse loss and cognitive decline in both mouse models of AD and human patients.

Material and methods

Mouse lines

The *Casp3*$^{-/-}$ mouse line was a generous gift from Dr. Richard Flavell. This mouse line was received as cryopreserved sperm and was rederived using C57Bl/6J oocytes. The resulting colony was maintained by continuous backcrossing to C57Bl/7J mice. We verified that mice in our *Casp3*$^{-/-}$ colony were congenic to the C57Bl/6J background (greater than 99% identity by SNP analysis). It is important to note that regular backcrossing is necessary to maintain phenotype stability in *Casp3*$^{-/-}$ mice. A small fraction of *Casp3*$^{-/-}$ mice displayed varying degrees of hydrocephalus. These animals were excluded from our analyses. *Cx3cr1-Gfp* mice (stock number 005582) were obtained from the Jackson laboratory. *Aldh1l1-Gfp* transgenic mice (stock number 011015-UCD) were obtained from Mutant Mouse Resource and Research Centers (MMRRC) as cryopreserved sperm and rederived using C57Bl/6J oocytes. *App/Ps1*mice were obtained from the Jackson laboratory (stock number 034832). Mice carrying *App/Ps1* transgenes were given DietGel® 76A (ClearH_2O, 72-07-5022) and were euthanized at the age of 6 months if not used in experiments. For experiments associated with **Figure 1** and **Figure 2**, C57Bl/6NCrl mice were obtained from Charles Rive Laboratories (strain code 027). For experiments associated with **Figure 6**, C57Bl/6J mice were obtained from the Jackson Laboratory (stock number 000664). All animal procedures were carried out according to IACUC approved protocols.

Reagents

Reagents were obtained from the following sources: isoflurane liquid (NDC 50989-150-15) was from Vedco; phosphate buffered saline without calcium and magnesium (PBS^-, BP2438) was from Fisher Scientific; bicuculline (0130) and cyclothiazide (0713) were from Tocris Bioscience; PBS with calcium and magnesium (PBS^+, SH30264) was from Cytiva; dimethyl sulfoxide (DMSO, D2650), bovine serum albumin (BSA, A9647), triton X-100 (T8787), Thioflavin S (T1892) were from Millipore-Sigma; paraformaldehyde powder (19200) was from Electron Microscopy Science; RPMI 1640 medium (11875093), DMEM medium (11965092), fetal bovine serum (FBS, 16000044), penicillin/streptomycin (pen/strep, 15140122), CD Hybridoma medium (11279023), GlutaMAX supplement (35050061), protein A/G agarose beads (20421), protein A/G IgG binding buffer (54200), IgG elution buffer (21004), 1M Tris-HCl pH 8.0 (15568025), 10% normal goat serum (50062Z), ProLong™ Gold mounting medium (P36934), Alexa Fluor 546 succinimidyl ester (A20002), cholera toxin subunit beta(CTB) conjugated to AlexaFlour (AF) 488, AF555, AF594 and AF647 (C22841,

C22842, C22843, C34778), goat anti-rabbit secondary antibodies conjugated to AF488plus (A32731), AF555plus (A32732), AF594plus (A32740), and AF647plus (A32733), goat anti-chicken secondary antibody conjugated to AF488plus (A32931), goat anti-guinea pig secondary antibody conjugated to AF488 (A11073) and AF594 (A11076) were from ThermoFisher Scientific; anti-cleaved caspase-3 antibody (9661) was from Cell Signaling Technologies; anti-GFP antibody (GFP-1010) was from Aves Lab; anti-MAP2 antibody (NB300-213) was from Novus Biologicals; anti-NeuN antibody (266004) was from Synaptic Systems; anti-RBPMS antibody (1832-RBPMS) was from PhosphoSolutions; anti-Iba1 (ab178846) and anti-Homer1 (Ab97593) antibodies were from Abcam; anti-Cd68 antibody (MCA1957) was from Bio-Rad; hybridoma line producing anti-SV2 antibody (clone name SV2) was from DSHB.

DNA cloning and AAV preparation

To make the pAAV-hSyn-mTurquoise2 plasmid, we ordered the DNA fragment for mTurqouise2[67] as a Gblock from IDT and cloned it via isothermal assembly into a linearized AAV expression plasmid (derived from pAAV-Syn-iCre; Addgene #122518) under the control of human synapsin promoter. To make the pAAV-hSyn-TeTxLC-P2A-mTurqouise2 plasmid, the tetanus toxin light chain (TeTxLC) sequence along with the P2A sequence (2A peptide from porcine teschovirus-1 polyprotein) at the 3' end was obtained via PCR from Addgene plasmid #129102 and fused in-frame with the mTurquoise2 DNA sequence in the same plasmid backbone as the pAAV-hSyn-mTurquoise2 plasmid. Note that in the main text, we used pAAV-hSyn-TeTxLC to refer to pAAV-hSyn-TeTxLC-P2A-mTurquoise2 because AAV carrying this plasmid induced very low levels of mTurquoise2 expression *in vivo*. When we needed endogenous florescence labeling, we chose to premix AAV carrying pAAV-hSyn-TeTxLC-P2A-mTurquoise2 with other AAVs expressing fluorescent proteins (at 1:1 ratio).

The pAAV-hSyn-tdTomato plasmid was cloned and provided by Janelia Viral Tools. The pAAV-CAG-GFP plasmid was previously made by Svoboda lab and is available as Addgene #28014.

The recombinant AAVs were prepared by Viral Tools of Janelia Core Services. Briefly, two days before transfection, 293T cells were seeded in three 150 mm T/C dishes at 1 x 10^7 cells/dish in DMEM medium supplemented with 10% FBS and cultured at 37 °C with 5% CO_2. The cells were transfected with 84 µg of pAAV plasmid, DJ capsid plasmid[68], and pHelper plasmid (Agilent 240071) at a ratio of 5:2:3 in polyethylenimine. After 6 to 8 hours, the cells were replenished with serum-free DMEM and further incubated for 3 days. The recombinant AAVs were collected from both the cells and supernatant and purified by two rounds of continuous cesium chloride density gradient centrifugation, dialyzed,

concentrated, and filter sterilized. Titer (genome copies per ml) was determined by digital PCR with primers targeting the ITR. For all in vivo experiments a titer of at least 10^{13} genome copies/ml was used.

Intraocular injections

In utero intraocular injections were performed as previously described[69] with modifications. Briefly, pregnant mouse females with embryos at E15 gestation were anesthetized by 3% isoflurane inhalation, abdomens shaved, eye lube applied to each eye, then transferred to a nose cone and set to maintenance level of 2% isofluorane inhalation anesthesia. Warm fluids (lactated Ringer's solution + 5% dextrose, Strategic Applications Inc.), Buprenorphine (0.1 mg/kg, Butler Animal Health), and Ketoprofen (5 mg/kg, Covetrus) were administered subcutaneously just prior to starting surgery. The animal was placed in dorsal recumbency, and the abdomen was cleansed using alternating swabs of 70% ethanol and 4% Chlorhexidine Gluconate (Molnlycke Health Care). A sterile drape was placed over the abdomen and using aseptic technique, the abdominal skin and wall were cut at midline, before gently removing the uterus from the abdomen. While keeping the uterus/embryos hydrated with warm saline sterile solution, the embryos were gently positioned with ring forceps to hold each embryo securely for injection. A previously filled glass pipette (Drummond Scientific), beveled to 30-40 μm at the opening was utilized to deliver constructs utilizing a pre-programmed Nanoject III microinjector (Drummond Scientific). 200-250 nl of AAVs prep was injected through the uterine wall and into each eye at a speed of 50nl per second. To confirm proper targeting within the eye, the AAV solution was pre-mixed with 0.05% Fast Green (Sigma Aldrich). After all injections were completed, the uterus/embryos were carefully placed back into the abdomen and the abdomen was flushed with warm sterile saline. The abdominal wall and skin were sutured, and Marcaine (Hospira) was applied subcutaneously below the skin incision. A small drop of Vetbond (3M) was applied to seal the skin incision. The animal was then removed from the anesthesia apparatus and allowed to recover on a heating pad before being placed back into a clean cage.

For intraocular injection at P4 and P9, pups with desired genotypes were anesthetized in an induction chamber filled with 2.5% - 3% isoflurane using a calibrated vaporizer. After the onset of anesthesia, isoflurane is reduced to 1.25%, and the mouse was removed from the chamber and placed under a dissection microscope. Proparacaine ophthalmic solution (0.5%, Sandoz, NDC 61314-016-01) was applied to each eye to be injected. A re-breathing nose cone was used to deliver 1.25% – 2% isoflurane throughout the procedure. A gentle blunt dissection was performed at each eyelid junction utilizing closed No.5 Dumont forceps (Fine Science Tools) to create a 2-3 mm opening. A 33-gauge sharp beveled needle attached to a Hamilton microliter syringe (Hamilton Company) was used to draw up CTB-AF solutions. Just prior to

injecting, the eye was proptosed and held securely in place by the Dumont forceps in preparation for injection. While holding the eye securely in place, the sclera was punctured with the Hamilton needle at the level of the ora serrata to inject 2.5 µL (for P9) or 2 µL (for P4) of desired CTB-AF solution into each eye. After the injection, eye lube was applied, the eye was allowed to move back into the socket, and the eyelids were gently pressed close to protect the eye. Pups were allowed to recover from anesthesia on a heated pad and put back into the cage with the dam.

Monoclonal antibody production and labeling

SV2 hybridoma cells were thawed and seeded in RPMI 1640 medium containing 10% FBS and 1% Pen/Strep at 0.3 million cells/ml and cultured in an incubator at 37 °C with 5% CO_2. After reaching 1×10^6 viable cells/ml density, the cells were diluted 1:2 by adding an equal volume of serum free CD Hybridoma medium supplemented with 4% GlutaMax^{Tm} and returned to the incubator. This dilution process was repeated 2 more times so that the cells reached 1×10^6viable cells/ml density in a mixed medium containing ~1% FBS. Cell viability obtained was at least 90%. The cells were then spun down at 150xG for 10 minutes and resuspended in complete CD Hybridoma medium at 5×10^5 cells/ml density. The cells were further expanded by adding more complete CD Hybridoma medium when cells reach 1×10^6 cells/ml density. Once the desired total volume is reached (typically 100 ml), cells were cultured for 2 weeks without medium change.

Culture supernatant containing SV2 antibody was cleared of hybridoma cells by centrifuging at 1000xG for 10 min. Cleared supernatant was diluted 1:1 with IgG binding buffer and passed through 1 ml of protein A/G agarose bead slurry (ThermoFisher 20421, corresponding to 500 ul of settled resin) packed in a gravity flow column. The column was washed with IgG binding buffer, and SV2 antibody was eluted in five 1 ml fractions using IgG elution buffer and immediately neutralized with 10% volume of 1M Tris-HCl, pH 8.0. Fractions with highest antibody concentration were pooled, desalted with Zeba columns (ThermoFisher 89891), and concentrated to ~1 mg/ml using Amicon centrifuge filters (Millipore UFC801024). After adding glycerol (25% final), antibodies were flash frozen in liquid nitrogen and kept at -80 °C.

To label the primary SV2 antibodies, we used Alexa Fluor 546 succinimidyl ester. Briefly, we buffer-exchanged and concentrated SV2 IgG to 3 mg/ml using Amicon filters (UFC501024 Millipore Sigma) in phosphate buffered saline that was brought to pH 8.3 with 100 mM $NaHCO_3$. Dimethyl sulfoxide-dissolved Alexa Flour 546 succinimidyl ester was gently mixed with the SV2 IgG at 10:1 molar ratio and incubated for two hours at room temperature on a rotating shaker. Alexa Fluor 546 labeled IgG were purified from

unreacted succinimidyl esters with the aid of PD MiniTrap Sephadex G-25 column (Cytiva 28918007) in PBS^- by gravity flow following the manufacturer's instructions. The degree of labeling was determined by spectrophotometry on Nanodrop One (ThermoFisher) by accounting for the Alexa Fluor 546 extinction coefficient at 554 nm and the corrected protein absorbance at 280 nm. Typically, a degree of labeling of 8-9 mols of dye per mol of protein was obtained. Labeled SV2 were aliquoted and flash-frozen in 25% glycerol for long term storage at -80 °C at a final concentration of approximately 0.75 mg/ml.

Immunohistochemistry

The mice were deeply anesthetized in a chamber filled with saturating isoflurane gas and transcardially perfused first with PBS^- and then with paraformaldehyde (PFA) solution (4% w/v in 20.3 mM NaH_2PO_4 and 79.7 mM Na_2HPO_4, pH = 7.4). The brains were removed and post-fixed in 4% PFA solution overnight at 4 °C with gentle shaking. Fixed brains were washed 3×15 minutes in PBS^- at room temperature and stored in PBS^- at 4 °C. For long term storage, fixed brains were cryoprotected in 30% Sucrose (w/v in PBS^-) for 72 hours and frozen in Tissue-Tek® O.C.T. compound (Sakura) and stored at -80 °C.

Brains stored in PBS^- were imbedded in 4% agarose, and coronal sections (50 um thick for mice younger than P10 or 40 μm thick for adult mice) were prepared using a vibratome (Leica VT 1200S). For brains frozen in O.C.T. compound, coronal sections were prepared using a cryostat (Leica 3050S). Sections were floated in 24-well plates in PBS^- and stored at 4 °C. For antibody staining, free-floating sections were first permeabilized/blocked in 10% normal goat serum containing 0.3% (w/v) triton X-100 for 1 hour. The sections were then incubated with primary antibodies diluted in staining buffer (PBS^+ containing 2% BSA w/v and 0.3% triton X-100) at 4 °C overnight with gentle agitation. Dilutions of primary antibodies were: anti-cleaved caspase-3, 1:500; anti-GFP, 1:2000; anti-MAP2, 1:1000; anti-NeuN, 1:500; anti-Iba1, 1:500; anti-Cd68, 1:500; anti-SV2, dilute to 2.5 μg/ml; anti-Homer1, 1:400. The sections were then washed 3×15 minutes in washing buffer (PBS^+ containing 0.1% triton X-100) and stained with appropriate fluorophore-conjugated secondary antibodies diluted in staining buffer for 3 hours at room temperature with gentle agitation. Secondary antibodies were always used at 1:500 dilution. The sections were washed 3×15 minutes in washing buffer, rinsed 3×5 minutes in PBS^+, and mounted onto glass slides (Fisher, 12-550-15). After air-drying completely, mounted sections were immersed in ProLong™ Gold and coverslipped (Fisher, 12-541-024). The sections were imaged after 24 hours of curing at room temperature. The sections were protected from light during the entire process.

To prepare whole-mount retinae, eyes were removed from PFA perfused mice and placed in PBS^-. The cornea was punctured with a #11 scalpel, and several anterior-to-posterior cuts were made on the sclera starting from the puncture. Intact retinae were isolated by tearing and peeling off the sclera along the cuts. 4 to 5 radial cuts were made on each retina to flatten the tissue. Isolated retinae were post-fixed for 15 minutes in 4% PFA solution at room temperature with gentle agitation and washed for 3×5 minutes in PBS^- at room temperature with gentle agitation. Free-floating retinae were then stained with primary (anti-RBPMS antibody, used at 1:200 dilution) and secondary (goat anti-guinea pig Alexa Fluor 594plus) antibodies and mounted onto glass slides as described above.

For staining of amyloid-β (Aβ) plaques, a 1% Thioflavin S stock solution (w/v, dissolved in ddH_2O) was diluted 100-fold in 50% ethanol (prepared by mixing pure ethanol and ddH_2O at 1:1 ratio) to create a 0.01% (w/v) working solution. The stock and working solutions were discarded after each use. Free-floating brain sections were dehydrated by washing 2×5 minutes in 50% ethanol, stained in 0.01% Thioflavin S solution for 8 minutes, washed for 2×5 minutes in 50% ethanol, then re-hydrated by washing 3×5 minutes in PBS^+. All staining steps were performed at room temperature with gentle agitation. The sections were protected from light throughout the procedure. Stained sections were then mounted and cured as described above.

Measuring synapse inactivation-induced caspase-3 activity

For experiments associated with **Figure 1** and **Figure S4**, E15 C57Bl/6NCrl mice were injected in the right eyes either with AAV carrying hSyn-mTurquoise2 (control group), or with a 1:1 mixture of AAV carrying hSyn-mTurquiose2 and AAV carrying hSyn-TeTxLC-P2A-mTurquoise2 (synapse inactivation group). At the age of P5, brains of both groups of mice were harvested and sectioned as described above. To quantify caspase-3 activity in the dLGN and the localization of activated caspase-3 relative to TeTxLC-expressing RGC axons (**Figure 1**), sections were stained with anti-cleaved caspase-3 antibody (using goat anti-rabbit AF594plus as the secondary) and anti-GFP antibody (using goat anti-chicken AF488plus as the secondary). Alternatively, sections were co-stained with anti-cleaved caspase-3 (using goat anti-rabbit AF647plus as the secondary) and anti-MAP2 antibody (using goat anti-rabbit AF488plus as the secondary) (**Figure S4A**), or with anti-cleaved caspase-3 (using goat anti-rabbit AF594plus as the secondary) and anti-NeuN antibody (using goat anti-rabbit AF488plus as the secondary) (**Figure S4C**). Immunostaining was performed as described above.

For experiments associated with **Figure 2**, E15 C57Bl/6NCrl mice were injected in the left eyes with AAV carrying hSyn-tdTomato and in the right eyes with AAV carrying CAG-eGFP (control group), or in the right

eyes with AAV carrying hSyn-mTurquoise2 and AAV carrying hSyn-TeTxLC-P2A-mTurquoise2 (single inactivation group), or in the left eyes with AAV carrying hSyn-tdTomato and AAV carrying hSyn-TeTxLC-P2A-mTurquoise2 and in the right eyes with AAV carrying CAG-eGFP and AAV carrying hSyn-TeTxLC-P2A-mTurquoise2 (dual inactivation group). At the age of P5, brains of all three groups of animals were harvested, sectioned, and stained with anti-cleaved caspase-3 antibody and goat antirabbit AF647plus secondary antibodies as described above.

To quantify caspase-3 activity in the dLGN (**Figure 1B-E**), confocal images of dLGNs were acquired on a Leica Stellaris 8 microscope using a 10x/0.4 NA dry objective (Leica HC PL Apo CS2 10x/0.4 dry). The channels were acquired sequentially (line-by-line) with the anti-caspase-3 first and anti-mTurquoise2 second. A 590 nm laser and emission read of 596 nm – 748 nm was used for the anti-cleaved caspase-3 channel, and 440 nm and 488 nm lasers and an emission read of 457 nm – 579 nm were used for anti-mTurquoise2 channel. The imaging parameters (laser power, pixel dwell time, signal averaging or accumulation) were set to maximize signal-to-background values while avoiding detector (SiPM type Power HyD S) saturation. Photon detection was set in counting mode and acquired as 12-bit images at 227 nm x 227 nm pixel size. All datasets used for measurement of caspase-3 activity were acquired as Z-stacks (7 slices spaced 2.4 μm apart). To measure the total amount of active caspase-3 signal in the 3D stacks of dLGN we used the Labkit[70] Fiji plugin to generate and train a pixel classifier through Imaris v. 10 (Oxford Instruments). The same pixel classifier and surface creation settings were applied to data from both the control and the synapse inactivation groups to generate surface objects of active caspase-3 signal. All active caspase-3 objects found within the dLGN area (manually delineated based on mTurquoise2 signal) were selected, and the sum of voxel intensities the active caspase-3 objects was calculated and divided by the area of dLGN. The final values plotted for each mouse are averages of two consecutive sections.

To image active caspase-3 signals and TeTxLC-expressing RGC axons at high resolution (**Figure 1G**), we used a Leica Stellaris 8 confocal microscope and a 63x/1.4 NA oil objective (Leica HC PL APO 63x/1,40 OIL CS2) in “Lightning” mode (in LasX 4.6) set at high resolution grade, which reduces the pinhole size to 0.5 Airy units. Laser and emission settings were identical to those used the previous section that described quantification of active caspase-3 signal in mTurquoise2-labeled dLGNs. 3D image stacks (31.5 um x 31.5 um x 12 um) were acquired at high voxel density (43 nm x 43 nm x 204 nm) in photon counting mode and 4x signal accumulation. Subsequently, the images were processed by iterative deconvolution using a theoretical point spread function informed by the imaging parameters of the microscope and constrained by an “Adaptive” strategy that accounts for local background and signal-to-noise ratio information.

Confocal images of MAP2 and active caspase-3 signals in dLGN (**Figure S4A**) were similarly imaged on a Leica Stellaris 8 microscope with a 63x/1.4 NA oil objective (Leica HC PL APO 63x/1,40 OIL CS2). A 653 nm laser line and an emission read of 662 nm – 829 nm were used for caspase-3 channel, and a 499 nm laser line and an emission read of 504nm – 549 nm were used for Map2 channel. The channels were acquired simultaneously at voxel densities of 65 nm x 65 nm x 299 nm. NeuN and active caspase-3 signals in dLGN (**Figure S4C**) were imaged using a 20x/0.7 NA water objective (Leica HC PL APO 20x/0,7 IMM CORR CS2). A 590 nm laser and an emission read of 595 nm – 750 nm were used for imaging caspase-3 and a 499 nm laser with a 509 nm - 595 nm emission read was used for the NeuN signal. The channels were acquired sequentially (active caspase-3 first) at pixel densities of 142 nm x 142 nm.

Measuring overlap of eye-specific territories in dLGN

For comparison between $Casp3^{+/+}$ and $Casp3^{-/-}$ animals (**Figure 3**), $Casp3^{+/-}$ males were bred to $Casp3^{+/-}$ females to generate $Casp3^{+/+}$ and $Casp3^{-/-}$ littermate pups. Pups were genotyped at birth. Before intraocular injection, lyophilized CTB-AF488 and CTB-AF594 powders were reconstituted in 1% DMSO in PBS^{-} to a final concentration of 5 mg/ml. CTB solutions were aliquoted and stored at -20 °C for later use. Thawed CTB solutions were discarded after each surgery. Intraocular injection of CTB-AF solutions was performed at the age of P9 as described above. CTB-AF488 was injected into left eyes and CTB-AF594 into right eyes. 24 hours after the injection, brains of P10 pups were harvested, and 50 um thick coronal sections prepared as described above.

Cured sections were imaged on a Zeiss AxioObserver Z.1 microscope equipped with an LSM 880 Airy scan detector and an EC Plan-Neofluar 10x objective (NA = 0.3). A 488 nm laser and a 499-544 nm detection window were used for CTB-AlexaFlour488, and a 594 nm laser and a 597-659 nm detection window were used for CTB-AlexaFlour594. Signals from the two channels were acquired sequentially into 16-bit images with a 0.4 µm x 0.4 µm pixel size. Laser power and detector gain settings were maintained at the same level for most images, with occasional adjustment to avoid saturation. One image per dLGN per section was acquired.

To quantify the overlap between contralateral-specific and ipsilateral-specific territories in the dLGN, we selected 7-8 sections per animal that span the majority of left dLGN of and analyzed their images in ImageJ. For each image, a mask for the entire dLGN region and a mask for a background region in the thalamus with no labeling were manually created. Background signal from each channel was estimated as the average signal in the background region and was subtracted from signals in the dGLN region. Then the

background-subtracted signals in the dLGN region were normalized to between 0 and 1 for each image and each channel. We picked 7 increasing cutoff thresholds (0.1,0.125,0.15,0.175,0.2,0.225, and 0.25), and for each threshold and each channel, signals that are greater than or equal to the threshold were considered real signals. For each animal (corresponding to 7-8 images of left dLGN) and each threshold, we calculated percentage overlap as the ratio between the total number of pixels with real signals in both channels in all images and the total number of pixels in the entire dLGN region of all images. We plotted the percentage overlap as a measurement of segregation of eye-specific territories in dLGN. Similar analyses were performed on right dGLN images yielding similar results.

For overlap analysis presented in **Figure S3**, E15 mouse embryos were injected in their right eyes either with AAV carrying hSyn-mTurqouise2 (control group) or a 1:1 mixture of AAV carrying hSyn-TeTxLC-P2A-mTurqouise2 and AAV carrying hSyn-mTurquoise2 (inactivation group). The left eyes of both groups of mice were injected with AAV carrying the hSyn-tdTomato. At P8, brains from both groups were harvested, and 50 μm thick coronal sections were prepared as described above. Only animals that had well labeled dLGNs on both sides were selected for analysis. Mounted and cured sections containing dLGN were imaged in confocal mode on a Leica Stellaris 8 microscope using a 10x/0.4 NA dry objective (Leica HC PL Apo CS2 10x/0.4 dry). A 441 nm laser and a 445-548 nm detection window were used for the mTurquoise2 channel, and a 554 nm laser and a 564-721 nm detection window were used for tdTomato channel. The images were acquired at 8-bit depth with a 0.227 μm x 0.227 μm pixel size (at 1 Airy unit for λ = 580 nm) and at a laser power, pixel dwell time, and signal accumulation sufficient to avoid detector (Power HyD S in counting mode) saturation. One image per dLGN per section was acquired. For each animal, overlap was measured as described above on the left dLGN (the side where mTurquoise2 signal occupied the majority of the dLGN) by averaging from 3 to 5 consecutive sections. The cutoff thresholds used were: 0.050, 0.075, 0.1, 0.125, 0.15, 0.175, 0.2.

For overlap analysis presented in **Figure S5**, embryos in the control group were injected at E15 with AAV carrying tdTomato construct in the left eyes, and with AAV carrying the CAG-GFP construct in the right eyes. Embryos in the dual inactivation group were injected at E15 with a mixture (1:1) of AAV carrying hSyn-tdTomato construct and AAV carrying hSyn-TeTxLC-P2A-mTurquoise2 construct in their left eyes, and with a mixture (1:1) of AAV carrying the CAG-GFP construct and AAV carrying the hSyn-TeTxLC-P2A-mTurquoise2 construct in their right eyes. At P10, the brains were harvested and sectioned as described above. Confocal images of dLGN were acquired on a Leica Stellaris 8 microscope using a 10x/0.4 NA dry objective (Leica HC PL Apo CS2 10x/0.4 dry). A 488 nm laser line with a 488 nm notch filter and a 485-559 nm detection window were used for the GFP channel, and a 554 nm laser and a 559-701 nm detection

window were used for the tdTomato channel in sequential line mode to avoid any cross-excitation (with tdTomato channel acquired first). The images were acquired at 12-bit depth with a 0.248 μm x 0.248 μm pixel size (at 1 Airy unit for λ = 580 nm) and at a laser power, pixel dwell time, and signal accumulation that avoided detector (Power HyD S in counting mode) saturation. One image per dLGN per section was acquired. For each animal overlap was measured as described above on the right dLGN (the side where tdTomato signal occupied the majority of the dLGN) by averaging from 5 consecutive sections.

Quantification of RGC densities in the retina

To estimate the density of RGCs in the retina (**Figure S6**), retinae of P10 *Casp3*$^{+/+}$ and *Casp3*$^{-/-}$ mice were harvested and stained with anti-RBPMS antibody as described above. We imaged 4 large square regions of interest (1.16 mm x 1.16 mm) in each retina on four sides of the optic disc. The images were acquired with a Leica TCS SP8 Laser Scanning Microscope using the 10x/0.4 NA dry objective (Leica HC PL Apo CS2 10x/0.4 dry), a 594 nm laser line, and an emission window of 607 nm to 694 nm, at a pixel sampling of 302 nm x 302 nm. To account for tissue unevenness, we collected a stack of 3 Z-slices (2.4 μm apart). To count RGCs, we sampled 3 subregions of a size of 100 μm^2 from each large region of interest. The subregions were selected to be at similar distances from the optic disc and in areas devoid of tissue tears. Cells were modeled to spots by fitting them to ellipsoid objects (XY size = 8 μm; Z size = 16 μm, with background subtraction) in Imaris 9.6 (Oxford Instruments). Densities of spots for each region were averaged and reported as number of RGC per 100 μm^2 of retina.

Whole-cell patch-clamp recording in acute brain slices

To characterize electrophysiological properties of retinogeniculate synapses in *Casp3*$^{+/+}$ and *Casp3*$^{-/-}$ mice (**Figure 4**), the mice (aged p28 – p32) were decapitated under deep isoflurane anesthesia, and the brain was removed and quickly transferred to an ice-cold dissection solution containing (in mM): 194 sucrose, 30 NaCl, 2.5 KCl, 1.2 NaH2PO4, 26 NaHCO3, 10 D-Glucose, 1 MgCl2 (pH 7.4, oxygenated with 95% CO2 and 5% O2). Parasagittal brain slices containing the optic tract and dLGN were prepared using a vibratome (Leica VT 1200S) as previously described[71][72]. The slices were recovered at 35.5°C in an incubation chamber (BSC-PC, Warner Instrument, USA) filled with artificial cerebrospinal fluid (ACSF) containing (in mM): 124 NaCl, 2.5 KCl, 1.2 NaH2PO4, 26 NaHCO3, 10 D-Glucose, 2 CaCl2, 1 MgCl2 (pH 7.4, oxygenated with 95% CO2 and 5% O2, osmolarity ~310). After ~30 minutes of recovery, the chamber was maintained at room temperature.

All recordings were performed with a MultiClamp 700B amplifier (Molecular Devices) and signals were filtered at 2 kHz and digitized at 20 kHz with via USB-6343 (National Instruments) under the control of WaveSurfer software (https://wavesurfer.janelia.org). All recordings were carried on slices submerged in the recording chamber of an upright microscope (BX61WI; Olympus, Tokyo, Japan) equipped with IR-DIC (infrared-differential interference contrast) microscopy and a water-immersion objective lens (60X, 1.00 NA; Olympus). Slices were maintained under continuous perfusion of oxygenated ACSF at 29-30°C. Patch pipettes were pulled from thin-wall single-barrel borosilicate glass (TW150-6, WPI), resulting in electric resistance of 2 ~ 5 MΩ when filled with an intracellular solution contained the following (in mM): 120 cesium methane sulfonate, 5 NaCl, 10 tetraethylammonium chloride, 10 HEPES, 4 lidocaine N-ethyl bromide, 1.1 EGTA, 4 magnesium ATP, and 0.3 sodium GTP, with pH adjusted to 7.2 with CsOH and osmolality set to ~290 mOsm.

Whole-cell voltage-clamp recordings of relay neurons in the dLGN were performed as previously described (**Figure 4A-C**)[72]. The slices were submerged in ACSF containing 20 uM bicuculline to inhibit $GABA_A$ receptors, and a bipolar concentric stimulation electrode (FHC) was placed on the surface of the optic tract to deliver stimuli with intensities ranged from 0 – 100 μA (200us duration) with an inter-trial interval of 40 – 60 s. In the whole-cell configuration (series resistance < 20 MΩ), the membrane potential of the neuron was clamped at -70 mV to measure evoked excitatory postsynaptic current (EPSC) mediated by activation of AMPA receptors, and then at +40 mV to measure evoked EPSC mediated by activation of NMDA receptors. The stimulus intensity was systemically increased until a response to the stimulus was observed, and then was reduced to a previous level where no response was detected. From that level, the stimulus intensity was increased by 0.5 μA steps to recruit single inputs which were putative single fiber (SF) amplitudes. When the EPSC amplitude reached a plateau, it was considered a putative maximum response. If the EPSC amplitude dropped while the stimulation intensity increased, data from that relay neuron was discarded.

To measure paired pulse ratio (PPR) (**Figure 4D-E**), the slices were submerged in the ACSF containing 20 uM bicuculline and 50 uM cyclothiazide to inhibit AMPAR desensitization, and the stimulation electrode was placed on the optic tract. In the whole-cell configuration, the membrane potential was clamped at -70 mV. After confirming the stimulation intensity that evoked the maximum response, two consecutive electrical stimuli of that intensity (300 μs duration) were delivered at 50, 150, 250, 500, and 1000 ms inter-stimulus intervals. Each pair of stimuli constitutes one trial, and two consecutive trials were separated by an interval of 40 s. For each inter-stimulus interval, two trials were performed and averaged. PPR was

calculated as the maximum amplitude of the second EPSC over the maximum amplitude of the first EPSC. If in any trial except for the first trial the first EPSC dropped significantly in amplitude compared to the first EPSC of the first trial, data from that dLGN relay neuron was discarded.

Measuring microglia- and astrocyte-mediated synapse engulfment in vivo

To measure microglia-mediated synapse engulfment *in vivo* (**Figure 5** and **Figure S10**), we bred *Casp3*$^{-/-}$ males to *Casp3*$^{+/-}$; *Cx3ct1-Gfp*$^{+/-}$females to generate *Casp3*$^{-/-}$; *Cx3ct1-Gfp*$^{+/-}$and *Casp3*$^{+/-}$; *Cx3ct1-Gfp*$^{+/-}$ littermate pups. To measure astrocyte-mediated synapse engulfment *in vivo* (**Figure S11**), we bred *Casp3*$^{-/-}$ males to *Casp3*$^{+/-}$; *Aldh1l1-Gfp*$^{+/-}$ to generate *Casp3*$^{-/-}$; *Aldh1l1-Gfp*$^{+/-}$ and *Casp3*$^{+/-}$; *Aldh1l1-Gfp*$^{+/-}$ littermate pups. P4 pups with desired genotypes were injected with 2 µL of CTB-AF555 in left eyes and 2 µL of CTB-AF647 in right eyes as described above. 24 hours later, the brains were harvested, sectioned, and mounted as described above.

To analyze engulfment of synapses, the sections were imaged using a Leica TCS SP8 Laser Scanning Microscope equipped with an HC Plan Apo CS2 40x (NA = 1.3) oil objective and a White Light Laser Unit. The 3D multichannel stacks with a voxel size of 0.075 x 0.075 x 0.312 µm for microglia samples or 0.048 x 0.048 x 0.2 µm for astrocytes samples were acquired as 16-bit images with 4x line averages for microglia or 2x for astrocytes at 400 Hz scanner speed. The stacks were set to collect a volume of 20 micrometers in the Z dimension and 387.5 micrometers in XY dimensions for microglia or 288 µm in XY for astrocytes. The pinhole was set at 1 Airy unit for 520 nm wavelength. The excitation lasers and detection windows were set to minimize crosstalk and bleed-through as well as the saturation of detectors while simultaneously imaging the three channels. A 478 nm laser and a detection window of 488 nm – 537nm were used for the GFP channel, a 550 nm laser and a detection window of 596 nm – 629 nm were used for CTB-AF555, and a 651 nm laser and a detection window of 665 nm to 750 nm were used for CTB-AF647. Imaris 9.6 (Oxford Instruments) was used to segment microglia, astrocytes, ipsilateral RGC axon terminals, and contralateral RGC terminals from the 3D stacks using the Surface Creation module with background subtraction. For segmentation of RGC axon terminals and astrocytes, all parameters used were left at default values (auto). For segmentation of microglia, we set the threshold manually at the highest inflection curve in the histogram of voxel intensities, which in our experience provided a good trade-off for good segmentation of cell bodies and major processes while keeping the adjustment consistent across different image datasets. A background subtraction ball size of 1 µm was used for microglia, a ball size of 1.4 µm was used for astrocytes, and a ball size of 0.5 µm was used for AF555 and AF647 labeled axonal materials. The

segmented signal of AF555 and AF647 was each converted to a binary mask of 0 and 1 voxels. Finally, the sum of the segmented volume (i.e. sum of ones) of AF555 and or AF647 in each microglia or astrocyte was either directly plotted or normalized to the microglia or astrocyte volume and plotted. To control the inherent signal variability across LGN, only microglia and astrocytes present in the ipsilateral region of the 3 middle sections of the left dLGN of each mouse were included in the analysis. Also, only microglia or astrocytes whose soma and proximal processes were contained in the volumetric stack were included in the final analysis. All littermate pups of the same genotype were pooled together.

Measuring activity-dependent engulfment of synapses by microglia

To investigate the role of caspase-3 in activity-dependent synapse elimination (**Figure 6** and **Figure S12**), we used C57Bl/6J wildtype mice as controls and bred *Casp3*$^{-/-}$ males with *Casp3*$^{+/-}$ females to generate *Casp3*$^{-/-}$ mice. Note that C57Bl/6J and *Casp3*$^{-/-}$ mice used in this experiment are not littermates and should not be directly compared with each other. C57Bl/6J and *Casp3*$^{-/-}$ embryos were injected at E15 in their right eye either with AAV carrying hSyn-TeTxLC-P2A-mTurqouise2 or AAV carrying hSyn-mTurquoise2 as described above. To label the RGC axons, at P4, the pups were injected with 2 µL of CTB-AF555 in left eyes and 2 µL of CTB-AF647 in right eyes as described above. At P5, the brains were harvested and sectioned. Two 50 µm sections that spanned the central part of the dLGN were stained with anti-Iba1 antibody and goat anti-rabbit AF488 secondary (as described above) to label microglial cell bodies.

Mounted and cured sections were then imaged on Leica Stellaris 8 confocal microscope using a 63x/1.4 NA oil objective (Leica HC PL APO 63x/1,40 OIL CS2). Four stitched 3D-stacks were acquired for each left dLGN (the side where CTF-AF647 and mTurquoise2 occupied the majority of the dLGN) to generate a 3D volume of 366 µm x 366 µm in XY and approximately 20 µm in the Z dimension, with a voxel size of 64 nm x 64 nm x 299 nm. The channels were acquired sequentially: first using a 499 nm laser with an emission window of 507-556 nm together with a 653 nm laser with an emission window of 663-750 nm for Iba1-AF488 and CTB-AF647 signal, respectively, then using a 553 nm laser with an emission window of 558-663 nm for the CTB-AF555 signal. Images acquired were collected as 12-bit datasets, and care was taken to set the laser power, signal accumulation, and pixel dwell time to avoid detector saturation. Only animals whose dLGN areas were fully labeled with both AF555 and AF647 as well as the mTurquoise signals were imaged and analyzed. Animals in which CTB signal appeared widespread throughout the brain parenchyma were excluded from the analysis as these labeling patterns were likely due to surgical mistargeting or issues with tissue integrity.

To segment volumes corresponding to microglia and CTB-AF555 and CTB-AF647 labeled RGC axon terminals, we utilized the Surface Creation module with machine learning segmentation of Imaris 10.1.1 (Oxford Instruments). We first trained for several rounds a pixel classifier for each channel using two independent image files and saved the classifiers along with the other settings (smoothing grain size of 100 nm and discarding volumes smaller than 10 voxels) as "Favorite Creation Parameter". Subsequently, the same Favorite Creation Parameters were applied to all data sets, with the rare instances when microglia segmentation was slightly tuned via the same pixel classier to better capture some of the cell border areas. Similar to the previous analyses (**Figure 5**), the segmented signals of CTB-AF647 and CTB-AF555 were converted to binary images (0 or 1 voxels), and the total volume of CTB-AF647- or CTB-AF555-positive voxels in each microglia was extracted, converted to fraction of the microglia volume, and plotted. Only the cells whose body and major processes were bound within the 3D stack and present within the middle area of dLGN (where the ipsilateral signal is present) were included in the analysis. Data from the same genotype and treatment were pooled together. Either one or two sections were analyzed for each animal.

Measuring microglia activation

To measure if lack of caspase 3 causes microglia activation (**Figure S9**), we bred *Casp3*$^{+/-}$males with *Casp3*$^{+/-}$ females to generate *Casp3*$^{-/-}$ and Casp3$^{+/+}$ littermates. After genotyping, at P5, the brains were harvested and sectioned coronally as described above. Two 50 μm sections that spanned the central part of the dLGN were stained with anti-Iba1 antibody (detected by goat anti-rabbit AF488 secondary) to label microglial cell bodies and anti-CD68 antibody (detected by donkey anti-rat AF555 secondary) to detect CD68 protein. Mounted and cured sections were imaged on Leica Stellaris 8 confocal microscope using a 63x/1.4 NA oil objective (Leica HC PL APO 63x/1,40 OIL CS2). A 3D image stack of 185 μm x 185 μm in XY and approximately 20 μm in the Z dimension, with a voxel size of 72 nm x 72 nm x 299 nm was acquired for each dLGN. The channels were acquired in photon counting mode simultaneously: a 499 nm laser with an emission window of 504-548 nm together with a 553 nm laser with an emission window of 560-650 nm for Iba1-AF488 and CD68-AF555. To eliminate any fluorescence emission bleed-trough between channels, the photon arrival times were gated to 3 - 5 ns for Iba1-AF488 and to 0 - 1.5 ns for Iba1-AF555 channels, respectively. Images acquired were collected as 8-bit datasets, and care was taken to set the laser power, signal accumulation, and pixel dwell time to avoid fluorophore bleaching or detector saturation.

For segmentation of microglia and CD68 signals, we utilized the Surface Creation module with machine learning segmentation of Imaris 10.1.1 (Oxford Instruments). We first trained for several rounds a pixel classifier for each channel then saved the classifiers along with the other settings (smoothing grain size of

145 nm and discarding volumes smaller than 10 voxels) as “Favorite Creation Parameter”. Subsequently, the same Favorite Creation Parameters were applied to all data sets, with the rare instances when microglia segmentation was slightly adjusted via the same pixel classier to better capture some of the cell border areas. Similar to the previous analyses (**Figure 5**), the segmented signals of CD68-AF555 were converted to binary images (0 or 1 voxels), and the total volume CTB-AF555-positive voxels in each microglia was extracted, converted to fraction of the microglia volume, and plotted. For measurement of relative CD68 intensity, the sum of CD68 signal was divided by the microglia volume. Only the microglia whose body and major processes were confined within the 3D stack were included in the analysis. All staining, imaging and analysis parameters were identically applied to all sections. Two sections were analyzed for each animal. Data from the same genotype and were pooled together.

Characterization of App/Ps1 transgenic mice

To detect Aβ deposition (**Figure S13A**), brains of 6 month-old female *App/Ps1*$^{-/-}$ mice, 5 month-old and 6 month-old male and female *App/Ps1*$^{+/-}$ mice, and 6 month-old female *Casp3*$^{-/-}$; *App/Ps1*$^{+/-}$ mice were harvested, sectioned, and stained with Thioflavin S as described above. Stained sections were imaged on a Leica Stellaris 8 microscope using a 10x/0.4 NA dry objective (Leica HC PL Apo CS2 10x/0.4 dry). A 460 nm laser line was used for excitation and a window of 469 nm - 600 nm was used for emission. Tile images (pixel size: 284nm x 284 nm) were collected and merged into one image spanning an entire coronal section in Las X 4.6 Navigator. To quantify the level of amyloid deposition in 6 month-old female *App/Ps1*$^{+/-}$ and *Casp3*$^{-/-}$; *App/Ps1*$^{+/-}$ mice (**Figure S13B**), the number of Thioflavin S-positive plaques was manually counted in a total of 3 sections per animal and averaged.

To investigate the role of caspase-3 in Aβ-induced synapse loss (**Figure 7**), *Casp3*$^{-/-}$ mice were bred to *App/Ps1*$^{+/-}$ mice to create *Casp3*$^{-/-}$; *App/Ps1*$^{-/-}$ and *Casp3*$^{-/-}$; *App/Ps1*$^{+/-}$ mice. Brains of 6 month-old female *App/Ps1*$^{-/-}$ and *App/Ps1*$^{+/-}$ littermates as well as *Casp3*$^{-/-}$; *App/Ps1*$^{-/-}$ and *Casp3*$^{-/-}$; *App/Ps1*$^{+/-}$ littermates were harvested, sectioned, and stained with anti-SV2 antibody (conjugated to AF546) and anti-Homer1 antibody (using goat anti-rabbit AF647 as the secondary) to label presynaptic and postsynaptic compartments, respectively. Stained sections were imaged on a Leica Stellaris 8 confocal microscope using a 63x/1.4 NA oil objective (Leica HC PL APO 63x/1,40 OIL CS2). To acquire a representative dataset, we focused on the molecular layer of the dentate gyrus of the hippocampus from both the left and right side of the brain and sampled 3 regions from each side, as shown in **Figure S14**. 3D-stacks (61.5 μm x 61.5 μm x 20 μm) were acquired with a voxel size of 64 nm x 64 nm x 298 nm. 561 nm and 638 nm laser lines were used

for excitation, 555 nm – 635 nm and 642 nm – 792 nm windows were used for emission reading, and appropriate notch filters were used for blocking the exciting laser lines. The channels were acquired as 8-bit data sets with detectors set in counting mode, and the lasers power, signal accumulation, and pixel dwell time set at levels that avoided detector saturation. To measure synapse number per unit volume, we first trimmed the raw 3D stacks to a stack of approximately 3.5 μm thickness on the side closest to the coverslip (to avoid any signal depletion the middle part of the section due to antibody penetration issues) and cropped out regions where large gaps (corresponding to blood vessels) devoid of Sv2 or Homer1 staining were present. The punctate signals of SV2 and Homer1 were fit in Imaris 10.1 (Oxford Instruments) to ellipsoids (500 nm in XY and 850 nm in Z for SV2; 400 nm in XY and 800 nm in Z for Homer1) with background subtraction ("Spot Creation"). Then we designated as "synapses" all Homer1 ellipsoids that were within 300 nm of a SV2 ellipsoid (center-to-center distance). For each animal, the total number of synapses in all 3D-stacks analyzed was divided by the total volume of all stacks analyzed and plotted as a single value.

To detect Aβ-induced microglia activation (**Figure S16**), brains of 6 month-old female *App/Ps1*$^{-/-}$, *App/Ps1*$^{+/-}$, and *Casp3*$^{-/-}$; *App/Ps1*$^{+/-}$ mice were harvested, sectioned, and stained with anti-Iba1 antibody (using goat anti-rabbit AF647plus as the secondary) and anti-Cd68 (using goat anti-rat AF555plus as the secondary) as labels of microglia cell body and microglial activation, respectively. Stained sections were imaged on a Leica Stellaris 8 confocal microscope using a 20x/0.7 NA water objective (Leica HC PL APO 20x/0,7 IMM CORR CS2). Tile images spanning the hippocampus were acquired at voxel sizes of 142 nm x 142 nm x 300 nm. A 548 nm laser line and a 554 nm – 634 nm emission window were used for the CD68-AF555 channel, and a 653 laser line and a 663 nm – 748 nm emission window were used for the Iba1-AF647 channel. Microgliosis could be detected as clusters of microglia with stubby processes and strong intracellular Cd68 signals (**Figure S16**).

To quantify Aβ-induced caspase-3 activity (**Figure S17**), brains of 4 month-old, 5 month-old and 6 month-old female *App/Ps1*$^{-/-}$ and *App/Ps1*$^{+/-}$ littermates were harvested, sectioned, and stained with anti-cleaved caspase-3 antibody (using goat anti-rabbit AF555plus as the secondary). Stained sections were imaged on a Leica Stellaris 8 confocal microscope using a 63x/1.4 NA oil objective (Leica HC PL APO 63x/1,40 OIL CS2). We sampled at least 2 regions of interest from the molecular layer of the dentate gyrus of the hippocampus on each side of the brain. 3D-stacks (92.26 μm x 92.26 μm x 22 μm) were acquired with a voxel size of 81 nm x 81 nm x 299 nm. A 561 laser line was used for excitation and an emission window of 550 nm – 728 nm was used for the active caspase-3 channel. To measure the number of caspase 3 objects in the dataset, we

first trimmed the 3D stacks to a volume where the signal is uniformly distributed (i.e. in focus) and segmented the objects using the “Surface creation” analysis in Imaris 10.1 (Oxford Instruments). The dataset was first smoothed by a two-pixel filter, then a ball size of 400 nm was used to find the objects with background subtraction. Only objects bigger than 10 and smaller than 2000 voxels were kept. Finally, the number of caspase 3 objects was divided by the volume of the 3D stack analyzed and reported per brain side (left or right) for each animal.

To measure the relative density of granule cells in the dentate gyrus (**Figure S16**), brains of 6 month-old female *App/Ps1*$^{-/-}$, *App/Ps1*$^{+/-}$, *Casp3*$^{-/-}$; *App/Ps1*$^{-/-}$, and *Casp3*$^{-/-}$; *App/Ps1*$^{+/-}$mice were harvested, sectioned, and stained with anti-NeuN antibody (using goat anti-mouse AF594plus as the secondary) to label neuronal nuclei. Stained sections were imaged on a Leica Stellaris 8 confocal microscope using a 20x/0.7 NA water objective (Leica HC PL APO 20x/0,7 IMM CORR CS2). 3D stacks of the dentate gyrus (581 μm x 581 μm x 30 μm) were acquired at voxel sizes of 160 nm x 160 nm x 1000 nm for each section and side (left and right) using a 594 nm laser and an emission window of 597 nm to 750 nm. The channels were acquired as 8-bit images with the detector set in counting mode, and the lasers power, signal accumulation, and pixel dwell time set at levels that avoided detector saturation. To count the number of nuclei, images were first rotated to position vertically the cortical side of the dentate gyrus. A maximum projection of the brightest two Z-slices was extracted from each 3D stack, and NeuN+ nuclei were manually counted within a rectangular region of interest (89 μm x 150 μm) that was positioned on the granule cell layer at 300 μm away from the tip of the gyrus.

Acknowledgements

We thank Crystall Lopez, Benjamin Gantz, and Brooke Groff for help with animal husbandry and breeding. We thank Sarah Lindo, Colin Morrow, Claire Boyer, and Rae Demars for help with surgery. We thank Monique Copeland, Amy Hu, Morgan Clarke, and Benjamin Foster for help with histology. We are also grateful to Sarah Kivimaki and the Viral Tools team of Janelia Core Services for help with AAV preparation. We thank Dr. Cagla Eroglu, Dr. Richard Axel, and Dr. David Clapham for comments on the manuscript. This work is supported by the Howard Hughes Medical Institute.

References

1. ^*Kano M, Hashimoto K. Synapse elimination in the central nervous system. Curr Opin Neurobiol. 19: 154–161 (2009).*

2. ^ a, b *Faust TE, Gunner G, Schafer DP. Mechanisms governing activity-dependent synaptic pruning in the devel oping mammalian CNS. Nat Rev Neurosci. 22: 657–673 (2021).*
3. ^ a, b *Riccomagno MM, Kolodkin AL. Sculpting neural circuits by axon and dendrite pruning. Annu Rev Cell Dev Biol. 31: 779–805 (2015).*
4. ^ *Katz LC, Shatz CJ. Synaptic activity and the construction of cortical circuits. Science. 274: 1133–1138 (1996).*
5. ^ *Hua JY, Smith SJ. Neural activity and the dynamics of central nervous system development. Nat Neurosci. 7: 327–332 (2004).*
6. ^ *Stevens B et al. The classical complement cascade mediates CNS synapse elimination. Cell. 131: 1164–1178 (2 007).*
7. ^ a, b, c, d, e, f, g, h *Schafer DP et al. Microglia sculpt postnatal neural circuits in an activity and complement-dep endent manner. Neuron. 74: 691–705 (2012).*
8. ^ a, b *Li T et al. A splicing isoform of GPR56 mediates microglial synaptic refinement via phosphatidylserine bin ding. Embo J. 39: e104136 (2020).*
9. ^ a, b *Scott-Hewitt N et al. Local externalization of phosphatidylserine mediates developmental synaptic pruni ng by microglia. Embo J. 39: e105380 (2020).*
10. ^ a, b, c, d *Chung WS et al. Astrocytes mediate synapse elimination through MEGF10 and MERTK pathways. Nat ure. 504: 394–400 (2013).*
11. ^ *Wilton DK, Dissing-Olesen L, Stevens B. Neuron-Glia Signaling in Synapse Elimination. Annu Rev Neurosci. 42: 107–127 (2019).*
12. ^ *Chung WS, Allen NJ, Eroglu C. Astrocytes Control Synapse Formation, Function, and Elimination. Cold Sprin g Harb Perspect Biol. 7: a020370 (2015).*
13. ^ *Li Q, Barres BA. Microglia and macrophages in brain homeostasis and disease. Nat Rev Immunol. 18: 225–2 42 (2018).*
14. ^ a, b *Paolicelli RC et al. Synaptic pruning by microglia is necessary for normal brain development. Science. 333: 1456–1458 (2011).*
15. ^ a, b *Yasuda M, Nagappan-Cheaar S, Johnson-Venkatesh EM, Umemori H. An activity-dependent determinant of synapse elimination in the mammalian brain. Neuron. 109: 1333–1349 e1336 (2021).*
16. ^ *Philips RL et al. The JAK-STAT pathway at 30: Much learned, much more to do. Cell. 185: 3857–3876 (2022).*
17. ^ a, b *McIlwain DR, Berger T, Mak TW. Caspase functions in cell death and disease. Cold Spring Harb Perspect Bi ol. 5: a008656 (2013).*

18. ^a, ^bLi Z et al. Caspase-3 Activation via Mitochondria Is Required for Long-Term Depression and AMPA Recept or Internalization. Cell. 141: 859–871 (2010).

19. ^a, ^b, ^c, ^dPark SY, Kim IS. Engulfment signals and the phagocytic machinery for apoptotic cell clearance. Exp M ol Med. 49: (2017).

20. ^Trouw LA, Blom AM, Gasque P. Role of complement and complement regulators in the removal of apoptotic cells. Mol Immunol. 45: 1199–1207 (2008).

21. ^Williams DW, Kondo S, Krzyzanowska A, Hiromi Y, Truman JW. Local caspase activity directs engulfment of dendrites during pruning. Nat Neurosci. 9: 1234–1236 (2006).

22. ^Kuo CT, Zhu S, Younger S, Jan LY, Jan YN. Identification of E2/E3 ubiquitinating enzymes and caspase activit y regulating Drosophila sensory neuron dendrite pruning. Neuron. 51: 283–290 (2006).

23. ^Simon DJ et al. A caspase cascade regulating developmental axon degeneration. J Neurosci. 32: 17540–17553 (2012).

24. ^a, ^bErturk A, Wang Y, Sheng M. Local pruning of dendrites and spines by caspase-3-dependent and proteaso me-limited mechanisms. J Neurosci. 34: 1672–1688 (2014).

25. ^a, ^b, ^c, ^d, ^e, ^f, ^g, ^h, ^i, ^jLiang L, Chen C. Organization, Function, and Development of the Mouse Retinogeniculate Synapse. Annu Rev Vis Sci. 6: 261–285 (2020).

26. ^a, ^b, ^c, ^d, ^ePenn AA, Riquelme PA, Feller MB, Shatz CJ. Competition in retinogeniculate patterning driven by sp ontaneous activity. Science. 279: 2108–2112 (1998).

27. ^a, ^b, ^c, ^dStellwagen D, Shatz CJ. An instructive role for retinal waves in the development of retinogeniculate co nnectivity. Neuron. 33: 357–367 (2002).

28. ^a, ^b, ^cYasuda M, Nagappan-Cheaar S, Umemori H. In utero intraocular AAV injection for early gene expression in the developing rodent retina. STAR Protoc. 2: 100742 (2021).

29. ^Schiavo G et al. Tetanus and botulinum-B neurotoxins block neurotransmitter release by proteolytic cleava ge of synaptobrevin. Nature. 359: 832–835 (1992).

30. ^Krahe TE, El-Danaf RN, Dilger EK, Henderson SC, Guido W. Morphologically distinct classes of relay cells exh ibit regional preferences in the dorsal lateral geniculate nucleus of the mouse. J Neurosci. 31: 17437–17448 (201 1).

31. ^Parnavelas JG, Mounty EJ, Bradford R, Lieberman AR. "The postnatal development of neurons in the dorsal l ateral geniculate nucleus of the rat: a Golgi study." J Comp Neurol. 171: 481–499 (1977).

32. ^McComb S, et al. "Efficient apoptosis requires feedback amplification of upstream apoptotic signals by effec tor caspase-3 or -7." Sci Adv. 5: eaau9433 (2019).

33. ^ a, b Nagappan-Cheaar S, Yasuda M, Johnson-Venkatesh EM, Umemori H. "The molecular signals that regulate activity-dependent synapse refinement in the brain." Curr Opin Neurobiol. 79: 102692 (2023).

34. ^ a, b Rossi FM, et al. "Requirement of the nicotinic acetylcholine receptor beta 2 subunit for the anatomical and functional development of the visual system." Proc Natl Acad Sci U S A. 98: 6453–6458 (2001).

35. ^ Kuida K, et al. "Decreased apoptosis in the brain and premature lethality in CPP32-deficient mice." Nature. 384: 368–372 (1996).

36. ^ a, b Houde C, et al. "Caspase-7 expanded function and intrinsic expression level underlies strain-specific brain phenotype of caspase-3-null mice." J Neurosci. 24: 9977–9984 (2004).

37. ^ a, b De Haan L, Hirst TR. "Cholera toxin: a paradigm for multi-functional engagement of cellular mechanisms (Review)." Mol Membr Biol. 21: 77–92 (2004).

38. ^ a, b, c, d Torborg CL, Feller MB. "Unbiased analysis of bulk axonal segregation patterns." J Neurosci Meth. 135: 17–26 (2004).

39. ^ Otsu N. "A Threshold Selection Method from Gray-Level Histograms." IEEE TransacGons on Systems, Man, and CyberneGcs. 9: 62–66 (1979).

40. ^ Young RW. "Cell death during differentiation of the retina in the mouse." J Comp Neurol. 229: 362–373 (1984).

41. ^ Dreher B, Potts RA, Benne MR. "Evidence that the early postnatal reduction in the number of rat retinal ganglion cells is due to a wave of ganglion cell death." Neurosci LeK. 36: 255–260 (1983).

42. ^ Rodriguez AR, de Sevilla Muller LP, Brecha NC. "The RNA binding protein RBPMS is a selective marker of ganglion cells in the mammalian retina." J Comp Neurol. 522: 1411–1443 (2014).

43. ^ a, b, c Chen C, Regehr WG. "Developmental remodeling of the retinogeniculate synapse." Neuron. 28: 955–966 (2000).

44. ^ a, b Hooks BM, Chen C. "Distinct roles for spontaneous and visual activity in remodeling of the retinogeniculate synapse." Neuron. 52: 281–291 (2006).

45. ^ a, b, c Regehr WG. "Short-term presynaptic plasticity." Cold Spring Harb Perspect Biol. 4: a005702 (2012).

46. ^ Jung S, et al. "Analysis of fractalkine receptor CX (3) CR1 function by targeted deletion and green fluorescent protein reporter gene insertion." Mol Cell Biol. 20: 4106–4114 (2000).

47. ^ Iram T, et al. "Megf10 Is a Receptor for C1Q That Mediates Clearance of Apoptotic Cells by Astrocytes." J Neurosci. 36: 5185–5192 (2016).

48. ^ Lemke G. "Biology of the TAM receptors." Cold Spring Harb Perspect Biol. 5: a009076 (2013).

49. ^Gong S, et al. "A gene expression atlas of the central nervous system based on bacterial artificial chromoso mes." Nature. 425: 917–925 (2003).

50. a, bKnopman DS, et al. "Alzheimer disease." Nat Rev Dis Primers. 7: 33 (2021).

51. ^Menah S, Gan J. "Alzheimer's disease as a synaptopathy: Evidence for dysfunction of synapses during diseas e progression." Front SynapGc Neurosci. 15: 1129036 (2023).

52. ^Shankar GM, et al. "Amyloid-beta protein dimers isolated directly from Alzheimer's brains impair synaptic plasticity and memory." Nat Med. 14: 837–842 (2008).

53. ^Jo J, et al. "Abeta (1-42) inhibition of LTP is mediated by a signaling pathway involving caspase-3, Akt1 and GSK-3beta." Nat Neurosci. 14: 545–547 (2011).

54. ^D'Amelio M, et al. "Caspase-3 triggers early synaptic dysfunction in a mouse model of Alzheimer's disease." Nat Neurosci. 14: 69–76 (2011).

55. ^Jankowsky JL, et al. "Mutant presenilins specifically elevate the levels of the 42 residue beta-amyloid peptid e in vivo: evidence for augmentation of a 42-specific gamma secretase." Hum Mol Genet. 13: 159–170 (2004).

56. ^Suzuki Y, Nakabayashi Y, Takahashi R. "Ubiquitin-protein ligase activity of X-linked inhibitor of apoptosis p rotein promotes proteasomal degradation of caspase-3 and enhances its anti-apoptotic effect in Fas-induced cell death." Proc Natl Acad Sci U S A. 98: 8662–8667 (2001).

57. ^Choi YE, et al. "The E3 ubiquitin ligase cIAP1 binds and ubiquitinates caspase-3 and -7 via unique mechanis ms at distinct steps in their processing." J Biol Chem. 284: 12772–12782 (2009).

58. ^Buffelli M, et al. "Genetic evidence that relative synaptic efficacy biases the outcome of synaptic competitio n." Nature. 424: 430–434 (2003).

59. ^Lee YI. "Developmental neuromuscular synapse elimination: Activity-dependence and potential downstrea m effector mechanisms." Neurosci LeK. 718: 134724 (2020).

60. ^Garrido C, et al. "Mechanisms of cytochrome c release from mitochondria." Cell Death Differ. 13: 1423–1433 (2006).

61. ^Damisah EC, et al. Astrocytes and microglia play orchestrated roles and respect phagocytic territories durin g neuronal corpse removal in vivo. Sci Adv. 6: eaba3239 (2020).

62. ^Eyo U, Molofsky AV. Defining microglial-synapse interactions. Science. 381: 1155–1156 (2023).

63. ^Suzuki J, Denning DP, Imanishi E, Horvitz HR, Nagata S. Xk-Related Protein 8 and CED-8 Promote Phosphat idylserine Exposure in Apoptotic Cells. Science. 341: 403–406 (2013).

64. ^Segawa K, et al. Caspase-mediated cleavage of phospholipid flippase for apoptotic phosphatidylserine expo sure. Science. 344: 1164–1168 (2014).

65. ^Gyorffy BA, et al. Local apoptotic-like mechanisms underlie complement-mediated synaptic pruning. Proc Natl Acad Sci U S A. 115: 6303–6308 (2018).

66. ^van Bokhoven P, et al. The Alzheimer's disease drug development landscape. Alzheimers Res Ther. 13: 186 (2021).

67. ^Goedhart J, et al. Structure-guided evolution of cyan fluorescent proteins towards a quantum yield of 93%. Nat Commun. 3: 751 (2012).

68. ^Grimm D, et al. In vitro and in vivo gene therapy vector evolution via multispecies interbreeding and retargeting of adeno-associated viruses. J Virol. 82: 5887–5911 (2008).

69. ^Yasuda M, Nagappan-Chettiar S, Umemori H. In utero intraocular AAV injection for early gene expression in the developing rodent retina. STAR Protoc. 2: 100742 (2021).

70. ^Arzt JDM, et al. LABKIT: Labeling and Segmentation Toolkit for Big Image Data. Frontiers in Computer Science. 4 (2022).

71. ^Turner JP, Salt TE. Characterization of sensory and corticothalamic excitatory inputs to rat thalamocortical neurones in vitro. J Physiol. 510 (Pt 3): 829–843 (1998).

72. a, bChen C, Regehr WG. Developmental remodeling of the retinogeniculate synapse. Neuron. 28: 955–966 (2000).

Declarations

Funding: No specific funding was received for this work.

Potential competing interests: No potential competing interests to declare.